The IRM Quarterly
Winter 2020, Vol. 30 No. 4
ISSN: 2152-1972

Inside...

Practical Magnetism V: another FORC in the road? Understanding, measuring, and interpreting FORC diagrams, part A

Dario Bilardello
Institute for Rock Magnetism
dario@umn.edu

Ramon Egli
Zentralanstalt für Meteorologie und Geodynamik (ZAMG)
ramon.egli@zamg.ac.at

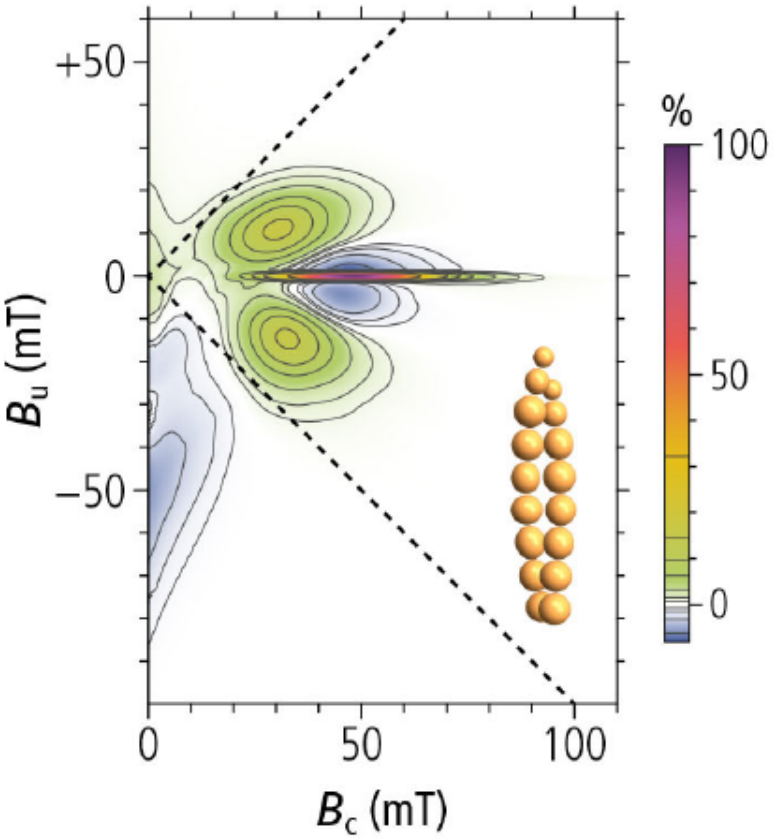

Simulated FORC diagram (Egli, 2021) of randomly oriented, double-stranded chains of equidimensional magnetosomes formed from the fold-collapse of single-stranded chains (example in the inset), data from Amor et al. (2021).

First-Order Reversal Curve (FORC) diagrams have become a sine qua non of modern rock-magnetism and are essential for the interpretation of magnetic mineralogies and their domain state. They aid paleomagnetic and paleointensity studies, for example, in investigating the stability of the magnetic carriers, and thus the reliability of the recorded paleomagnetic signals. They also have become an essential tool for identifying specific magnetic particle populations, such as magnetofossils. Despite their increasing popularity, interpreting FORC diagrams and even setting the correct measurement protocol parameters is not necessarily straight-forward, so that the nuances of these diagrams are not as readily accessible. A previous Quarterly article ("A FORC in the road?" by Chen et al., (2005), IRMQ 15-3) already dealt with FORC diagrams, however from a very different perspective. This article aims at providing a solid foundation for making informed interpretations by describing the features of FORC diagrams in the hopes of providing an "all in one" practical guide, rather than covering all the necessary phenomenological explanations that are already treated in greater detail elsewhere. That said, to discuss FORCs one must start in the neighborhood of the beginning, so a basic explanation will be provided. Likewise, correct interpretation of FORC diagrams is dependent on correct data acquisition and processing, therefore some of the most important measurement aspects will be covered. This "review" article takes widely from a number of publications, but if asked to recommend an essential bibliography on FORCs, we would probably suggest starting from Egli and Winklhofer (2014), Roberts et al. (2014), and Egli (2021). Because of the amount of material covered, the article will be split in two parts: the first providing background information and describing FORC signatures for the different domain states, from unstable single domain to multi domain, and the second describing the signatures for mixtures and different mineralogies.

What are FORC diagrams?

Before answering this question, we recall some fundamental aspect of magnetic measurements applied to natural magnetic particle assemblages, such as those oc-

cont'd. on pg. 10...

Visiting Fellow Reports

Testing the universality and scale of the magnetic hydrocarbon migration hypothesis-Catcher Area Development, Western shelf, UK North Sea

Maryam Abdulkarim
Imperial College, London
m.abdulkarim18@imperial.ac.uk

In my research group, we have been trying to determine the applicability of intra-sedimentary magnetic methods to hydrocarbon exploration and production. In general, the uncertainties involved in hydrocarbon exploration is significant. This is due to the complexity of the petroleum system and processes in play. Our aim is to reduce these uncertainties by the application of novel magnetic methods to the identification of hydrocarbon migration pathways. The magnetic signatures around hydrocarbon migration pathways compared to the surrounding background sediments have for a long time been suggested to be variant (e.g. Machel, 1995; Liu et al., 2004). However, no model that defines this variation of signature in a way that can be applied to improving the hydrocarbon exploration and production process has been developed. My research group makes progress here. There appears to be a relationship between hydrocarbon migration direction and the precipitation of siderite (Badejo et al., 2020). The implication of this finding includes the potential to incorporate a magnetic parameter to Petroleum Systems Modelling software to enhance their predictability.

My study objectives include testing the migration direction hypothesis and defining its applicability. To achieve this, sandstone samples from cores of a study area in the West Central Shelf of the UK North Sea were collected for magnetic experiments. These cores were collected along the hydrocarbon fill spill chain of a recent Tertiary hydrocarbon field development; the Catcher Area Development (CAD). Background sandstone samples of the same formation; unstained by hydrocarbon and located away from the migrating pathway of oil and gas were also collected. Hysteresis loops were obtained for these oil-stained and background samples at a high resolution; every meter, along the available core. These loops revealed the presence of significantly higher paramagnetic proportion in a significant number of oil-stained sandstone samples when compared to the background samples. Also, trends were observed in the distribution of the paramagnetic proportion along the fill spill chain. To understand the mineralogical distribution along this fill spill chain, I had previously carried out thermomagnetic and Mossbauer measurements on a small subset of the samples collected, through an earlier fellowship at the IRM. Analysis of these results revealed the presence of siderite, magnetite, pyrrhotite, haematite and titanium rich iron-oxides in various proportions in the oil-stained samples. The minerology of the background samples was less complex, with all the samples showing signs of magnetite, hematite and titanium-rich iron-oxides. The background sandstone's magnetic signature appears to be dominated by the presence of magnetite. We thus inferred the following: siderite and pyrrhotite were formed as a result of hydrocarbon migration and siderite was the source of the high paramagnetic proportion observed in some of the CAD samples.

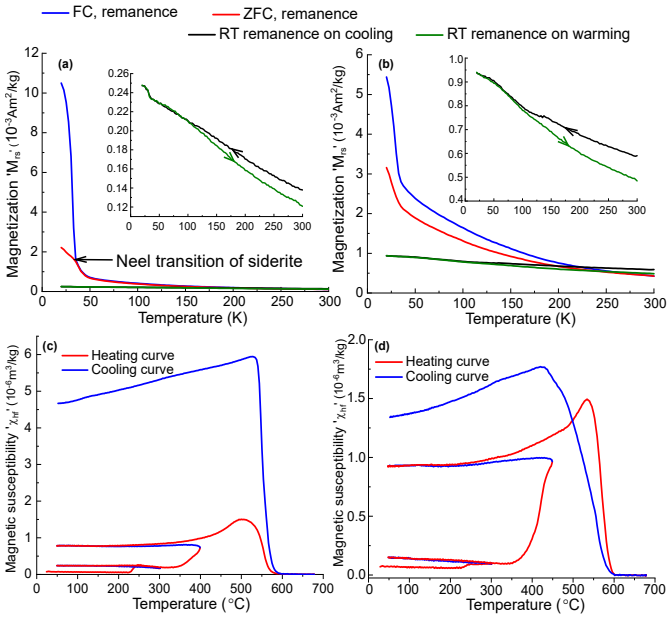

Figure 1: Thermomagnetic experimental results for (a & c) an oil stained sandstone and (b & d) a background sample. Siderite is clearly identified via its Neel's transition at 37 K from the FC-ZFC curves (Jacobs, 1963). The presence of siderite is further supported by the high susceptibility curves. Rapid alteration of siderite occurs at temperatures above 300 °C as it oxidizes to magnetite (Pan et al., 2000).

The main objectives of this second visiting fellowship were firstly, to determine through thermomagnetic studies if the trend in paramagnetic response can suggest the presence of siderite in the oil-stained sandstone samples. The number of samples measured were not enough to establish whether a trend, if any, existed. Paramagnetic clays like illite, smectite, illite-smectite etc are common in North Sea sandstones (Wilkinson et al., 2014) and could be a major contributor to the paramagnetic response. The second objective was to confirm the absence or negligibility of siderite in the background sample by carrying out mineralogical analysis on the samples with the highest paramagnetic response.

The results of the thermomagnetic experiments revealed the presence of siderite in all the samples above a threshold high field susceptibility. Siderite was identified via its Néel transition from the FC-ZFC curves (Fig. 1a). Its presence was also suggested by the rapid and substantial alteration of the samples during high temperature susceptibility measurements carried out in Argon environment (Fig. 1c). Siderite presence was also confirmed

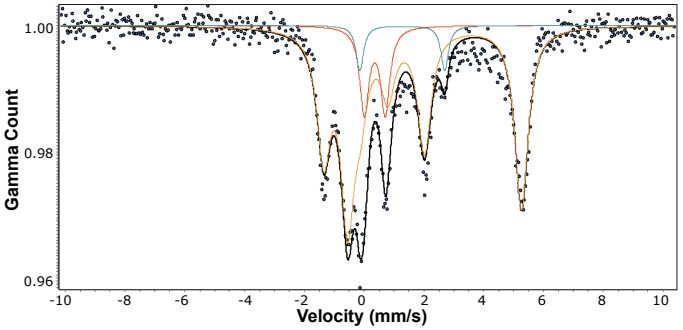

Figure 2: Low temperature Mössbauer spectroscopy results for oil stained CAD samples. The sextet's parameters fit to siderite with isomer shift 'IS', quadrupole shift 'QS', and hyperfine field of 1.34 mm/s, 2.02 mm/s and 18.04 T respectively.

via Mössbauer spectroscopy (Fig. 2). Furthermore, we confirmed the negligibility of siderite in the background samples. Figs. 1(b) and 1(d) are thermomagnetic curves for the most paramagnetic background sample. The FC-ZFC curves (Fig 1b) do not show signs for the presence of siderite, as was the case in the oil-stained sandstone FC-ZFC curve (Fig. 1a) even though both samples have a high paramagnetic proportion (Find high field susceptibility values in Figs. 1(a) and 1(b)).

A comparison of the high field susceptibility (χhf) of the oil-stained samples with high paramagnetic proportion and their FC-ZFC curves suggests that siderite is the major contributor to the high paramagnetic proportion. The example curves in Fig. 3 depict this clearly. The signature of these curves strongly suggest the dominant paramagnetic mineral to be siderite with the wide separation between the FC-ZFC curves, which occurs sharply below siderite's Neel temperature of 37 K. Superimposing this inference with the trends in the high field susceptibility and the FC-ZFC remanence, it appears that in this region, high field susceptibility can be used to estimate the variation of siderite along the fill spill chain.

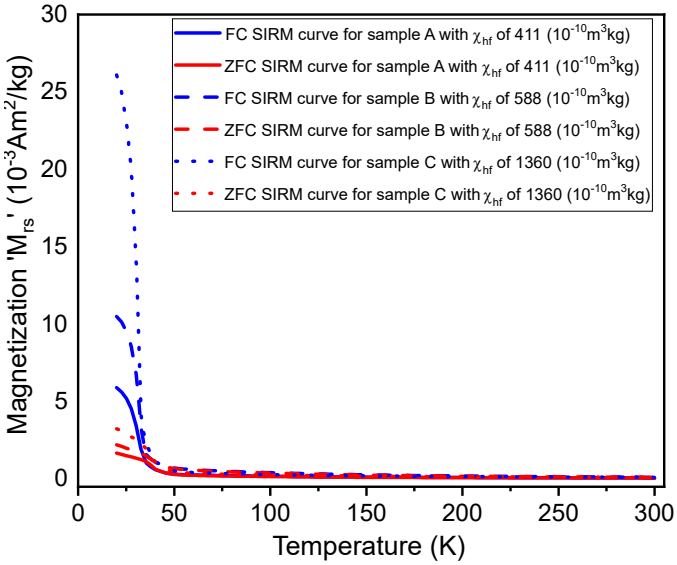

Figure 3: Comparison of the ZFC-FC curves for different oil-stained samples with different paramagnetic proportions. Each sample's FC-ZFC curve shows clear indications for the presence of siderite. Comparing the signature and magnitude of magnetization to the high field susceptibility suggests that siderite is the major contributor to the high paramagnetic proportion.

Acknowledgement

A big thank you to the Institute for Rock Magnetism (IRM) for the fellowship that allowed me to obtain these data. I would also like to thank Max, Dario and Peat for all their assistance which included carrying out all the measurements due to COVID restrictions. Thanks also to Josh and Bruce for their valuable suggestions.

References

Badejo, S. A., Muxworthy, A. R., Fraser, A., Neumaier, M., Stevenson, G. R., & Davey, R. (2020). Using magnetic technique to calibrate hydrocarbon migration in petroleum systems modelling: A case study from the Lower Tertiary, UK Central North Sea. Marine and Petroleum Geology, in review.

Jacobs, I. S. (1963). Metamagnetism of Siderite (FeCO3). Journal of Applied Physics, 34(4), 1106–1107.

Machel, H. G. (1995). Magnetic mineral assemblages and magnetic contrasts in diagenetic environments — with implications for studies of palaeomagnetism, hydrocarbon migration and exploration. Geological Society, London, Special Publications, 98(1), 9–29. https://doi.org/10.1144/gsl.sp.1995.098.01.02

Pan, Y., Zhu, R., Banerjee, S. K., Gill, J., & Williams, Q. (2000). Rock magnetic properties related to thermal treatment of siderite: Behavior and interpretation. Journal of Geophysical Research: Solid Earth, 105(B1), 783–794. https://doi.org/10.1029/1999jb900358

Qingsheng Liu, Lungsang Chan, Qingsong Liu, Haixia Li, Fang Wang, Shuangxi Zhang, … Tongjin Cheng. (2004). Relationship between magnetic anomalies and hydrocarbon microseepage above the Jingbian gas field, Ordos basin, China. American Association of Petroleum Geologists Bulletin, 88(2), 241–251.

Wilkinson, M., Haszeldine, R. S., & Fallick, A. E. (2014). Authigenic illite within northern and central North Sea oilfield sandstones: evidence for post-growth alteration. Clay Minerals, 49(2), 229–246. https://doi.org/10.1180/claymin.2014.049.2.06

A Rock Magnetic Study on Southwest Indian Ridge Basalt Hydrothermal Alteration

Shishun Wang
School of Earth and Space Sciences, Peking University, Beijing, China
wangshishun@pku.edu.cn

Hydrothermal alterations are frequently recognized when drilling the ocean crust (e.g., Ocean Drilling Program (ODP) Hole 1256D, Dekkers et al., 2014). There are two categories of hydrothermal systems: low-temperature (<200°C) fluids generated by cooling of the ocean lithosphere and high-temperature (250-400°C) vents above magma chambers along the mid-ocean ridges (Alt, 1995). High-temperature vents severely destroy the thermal remanent magnetization (TRM) of mid-ocean ridge basalts (MORB), resulting in negative magnetic anomalies (Tivey & Johnson, 2002). Although this signature

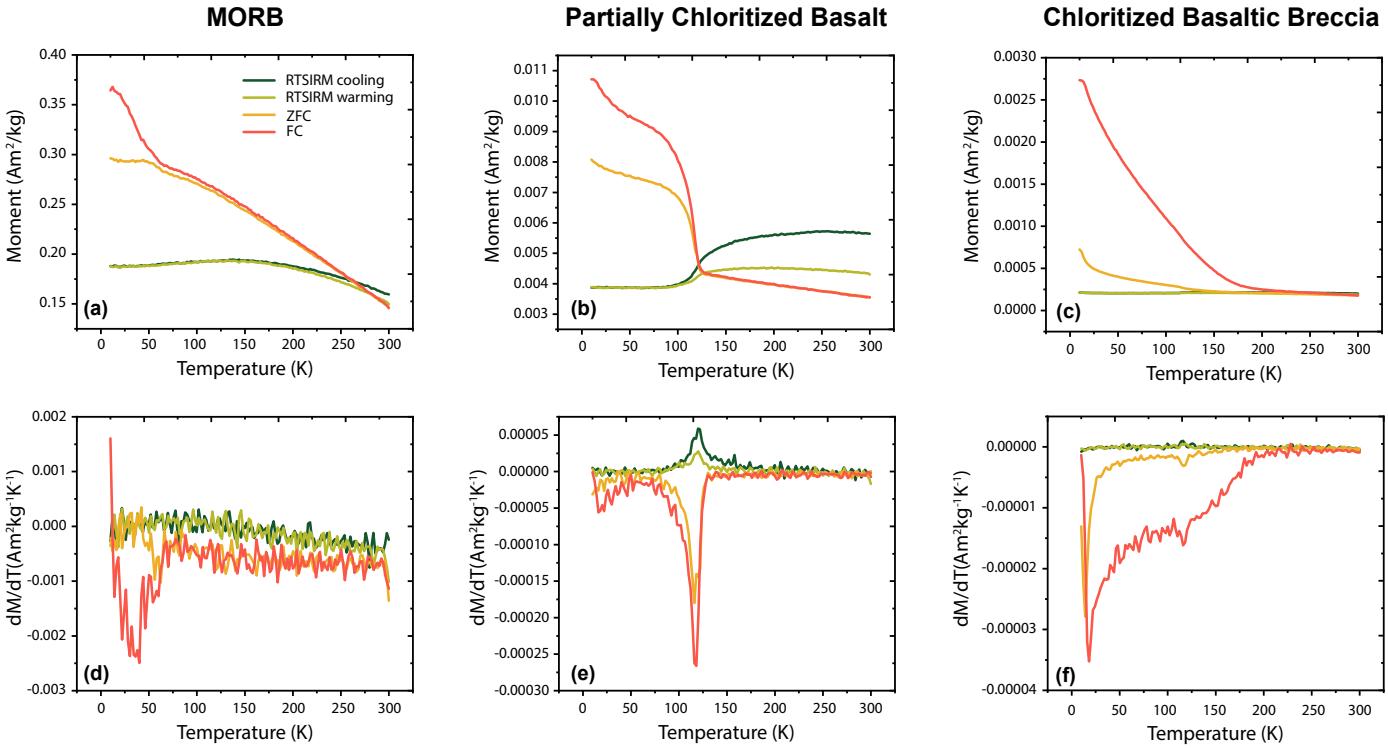

Figure 1: Low-temperature magnetic properties for MORB (a, d), partially chloritized basalt (b, e), and chloritized basaltic breccia (c, f). The lower panels (d-f) are the first derivative of the raw data (a-c). The low-temperature cycling of a room-temperature remanence (RTSIRM cooling and warming; green), as well as field-cooled (FC) and zero field-cooled (ZFC) remanence warming curves (red and orange), were measured.

has been widely applied in studying the internal structure of the vents (e.g., Galley et al., 2020), how fluid-rock interaction alters the magneto-mineralogy remains vague. My Ph.D. project is to study dredged basaltic samples from Longqi and Yuhuang hydrothermal vents at the Southwest Indian Ridge, which provides a chance to understand the interaction between hydrothermal fluids and basaltic ocean crust. Based on multi-scale microscopic analyses, we found that fresh MORBs were chloritized and brecciated when interacting with hydrothermal fluids. Primary titanomagnetites were dissolved by the fluids, reducing MORB's natural remanent magnetization (NRM) by three to four orders of magnitude (Wang et al., 2020). Following those findings, we aim to investigate how rock magnetic properties are modified by chloritization and brecciation during progressive hydrothermal alteration.

I applied for an IRM visiting fellowship to perform low-temperature measurements using the Quantum Design Magnetic Property Measurement System (MPMS) and Mössbauer spectra measurements. Combined with other rock magnetic data already obtained, these experiments were designed to characterize the properties of major lithological units (i.e., MORB, partially- and fully-chloritized basalts, and chloritized basaltic breccias) and assess their relationship to hydrothermal processes. Due to the COVID-19 pandemic, the samples were sent to the IRM and the measurements were conducted by the IRM personnel.

Here, I show primary low-temperature magnetic data of MORBs, partially chloritized basalts, and fully-altered chloritized basaltic breccias (Fig. 1). These three lithologies have systemic trends in terms of low-temperature phase transition: as expected, no phase transition is recognized in MORBs containing TM50-60 titanomagnetites, whereas partially chloritized basalts and chloritized basaltic breccias distinctly show the magnetite Verwey transition. Interestingly, the Verwey transition in partially chloritized basalts presents a bimodal distribution – a broad peak around 80-110 K and a sharp peak near 110-120 K. Our primary speculation is that the titanomagnetites in MORBs experienced high-temperature oxidation during alteration, producing pure magnetite that exhibits 110-120 K sharp peak. The broad 80-110 K peak could be related to less stoichiometric oxidation relicts. The chloritized basaltic breccias have less prominent Verwey peaks superimposed on the large separation of ZFC and FC curves, which indicates that the magnetite is transformed to other phases during later stages of alteration. Detailed data analyses will establish a link between rock magnetic and mineralogical properties and our microscopy observations.

With solid support from the IRM, I obtained valuable low-temperature and Mössbauer data, which helps me to proceed with my research under such a global crisis. I would like to thank Dr. Mike Jackson and Dr. Maxwell Brown for coordinating my experiment schedules and Dr. Dario Bilardello and Dr. Peter Solheid for their suggestions and for conducting the experiments.

References

Alt, J. C. (1995). Subseafloor processes in mid-ocean ridge hydrothermal systems. In S. E. Humphris et al. (Eds.), Seafloor hydrothermal systems: physical, chemical, biological, and geological interactions, Geophysical Monograph Series (vol. 91, pp. 85-114). Washington, DC: American Geophysical Union. https://doi.org/10.1029/GM091p0085

Dekkers, M. J., Heslop, D., Herrero-Bervera, E., Acton, G., & Krasa, D. (2014). Insights into magmatic processes and hydrothermal alteration of in situ superfast spreading ocean crust at ODP/IODP site 1256 from a cluster analysis of rock magnetic properties. Geochemistry, Geophysics, Geosystems, 15. https://doi.org/10.1002/2014GC005343

Galley, C. G., Jamleson, J. W., Lellèvre, P. G., Farquharson, C. G., & Parlanos, J. M. (2020). Magnetic imaging of subseafloor hydrothermal fluid circulation pathways. Science Advances, 6(44), eabc6844. https://doi.org/10.1126/sciadv.abc6844

Tivey, M. A., & Johnson, H. P. (2002). Crustal magnetization reveals subsurface structure of Juan de Fuca ridge hydrothermal vent fields. Geology, 30(11), 979–982. https://doi.org/10.1130/0091-7613(2002)030<0979:CMRSSO>2.0.CO;2

Wang, S., Chang, L., Wu, T., & Tao, C. (2020). Progressive dissolution of titanomagnetite in high-temperature hydrothermal vents dramatically reduces magnetization of Basaltic Ocean crust. Geophysical Research Letters, 47, e2020GL087578. https://doi.org/10.1029/2020GL087578

Visiting Fellows

January - June, 2021

Claudio Robustelli Test

Università degli Studi di Torino

Magnetic properties as a function of fluid-rock interaction at plate boundary shear zones

Maryam Abdulkarim

Imperial College

Testing the universality and scale of magnetic hydrocarbon migration hypothesis – Lower Tertiary reservoir systems, UK North Sea

Current Articles

A list of current research articles dealing with various topics in the physics and chemistry of magnetism is a regular feature of the IRM Quarterly. Articles published in familiar geology and geophysics journals are included; special emphasis is given to current articles from physics, chemistry, and materials-science journals. Most are taken from ISI Web of Knowledge, after which they are subjected to Procrustean culling for this newsletter. An extensive reference list of articles (primarily about rock magnetism, the physics and chemistry of magnetism, and some paleomagnetism) is continually updated at the IRM. This list, with more than 10,000 references, is available free of charge. Your contributions both to the list and to the Current Articles section of the IRM Quarterly are always welcome.

Archaeomagnetism

Duval, M., P. Voinchet, L. J. Arnold, J. M. Pares, W. Minnella, V. Guilarte, M. Demuro, C. Falgueres, J. J. Bahain, and J. Despriee (2020), A multi-technique dating study of two Lower Palaeolithic sites from the Cher Valley (Middle Loire Catchment, France): Lunery-la Terre-des-Sablons and Brinay-la Noira, Quaternary International, 556, 79-95, doi:10.1016/j.quaint.2020.05.033.

Garcia-Redondo, N., M. Calvo-Rathert, A. Carrancho, and M. Bustamante-Alvarez (2020), New high precision full-vector archaeomagnetic data from a roman kiln in Merida (Spain), Physics of the Earth and Planetary Interiors, 309, doi:10.1016/j.pepi.2020.106591.

Jordanova, N., D. Jordanova, E. Tcherkezova, H. Popov, A. Mokreva, P. Georgiev, and R. Stoychev (2020), Identification and Classification of Archeological Materials From Bronze Age Gold Mining Site Ada Tepe (Bulgaria) Using Rock Magnetism, Geochemistry Geophysics Geosystems, 21(12), doi:10.1029/2020gc009374.

Madingou, B. T., G. Herve, M. Perrin, F. N. M'Mbogori, D. Guemona, P. E. Mathe, P. Rochette, D. Williamson, V. Mourre, and C. Robion-Brunner (2020), First archeomagnetic data from Kenya and Chad: Analysis of iron furnaces from Mount Kenya and Guera Massif, Physics of the Earth and Planetary Interiors, 309, doi:10.1016/j.pepi.2020.106588.

Schnepp, E., D. Thallner, P. Arneitz, and R. Leonhardt (2020), New archeomagnetic secular variation data from Central Europe, II: Intensities, Physics of the Earth and Planetary Interiors, 309, doi:10.1016/j.pepi.2020.106605.

Databases

Bar, K., T. Reinsch, and J. Bott (2020), The PetroPhysical Property Database (P-3) - a global compilation of lab-measured rock properties, Earth System Science Data, 12(4), 2485-2515, doi:10.5194/essd-12-2485-2020.

Environmental Magnetism

Badesab, F., P. Dewangan, and V. Gaikwad (2020), Magnetic Mineral Diagenesis in a Newly Discovered Active Cold Seep Site in the Bay of Bengal, Frontiers in Earth Science, 8, doi:10.3389/feart.2020.592557.

Badesab, F., P. Dewangan, V. Gaikwad, J. G. Sebastian, and M. Venkateshwarlu (2020), A rock magnetic perspective of gas hydrate occurrences in a high-energy depositional system in the Krishna-Godavari basin, Bay of Bengal, Geo-Marine Letters, 40, 525–539, doi:10.1007/s00367-020-00646-8.

Bogalo, M. F., B. Bradak, J. J. Villalain, M. Calvo-Rathert, M.

I. Gonzalez, F. Heller, A. I. Ortega, and J. M. Pares (2021), High-resolution late Middle Pleistocene paleoclimatic record from the Galeria Complex, Atapuerca archaeological site, Spain - An environmental magnetic approach, Quaternary Science Reviews, 251, doi:10.1016/j.quascirev.2020.106721.

Chen, T., Q. S. Liu, Y. Zheng, and L. Y. Zhou (2020), Correlation patterns between magnetic parameters and heavy metals of core sediments in the Yellow River Estuary and their environmental implications, Marine Pollution Bulletin, 160, doi:10.1016/j.marpolbul.2020.111590.

Ebert, Y., R. Shaar, E. J. Levy, X. Zhao, A. P. Roberts, and M. Stein (2020), Magnetic Properties of Late Holocene Dead Sea Sediments as a Monitor of Regional Hydroclimate, Geochemistry Geophysics Geosystems, 21(11), doi:10.1029/2020gc009176.

Font, E., T. Adatte, A. Abrajevitch, J. Mirao, N. Sharma, V. Sordet, and M. Andrade (2020), Integrated mineralogical and rock magnetic study of Deccan red boles, in Mass Extinctions, Volcanism, and Impacts: New Developments, edited by T. Adatte, D. P. G. Bond and G. Keller, pp. 199-222, doi:10.1130/2019.2544(08).

Garnier, J. M., J. Garnier, P. Debnath, L. F. Prado, E. Yokoyama, R. K. Das, P. E. Mathe, and M. S. Islam (2020), Late Holocene paleoenvironmental records in Eastern Bangladesh from lake sediments: A multi-proxy approach, Quaternary International, 558, 39-46, doi:10.1016/j.quaint.2020.06.049.

Guo, S. L., Y. F. Cai, J. Ren, Y. X. Guan, D. C. Xin, and X. Y. Long (2021), Formation and migration of magnetic particles associated with iron oxide transformation at a hillslope scale, Catena, 197, doi:10.1016/j.catena.2020.104944.

Herrero-Bervera, E., Gerstnecker, K., Lopez, V., and B. Swilley (2020), Rock Magnetic Characterization of Fine Particles from Car Engines, Brake Pads and Tobacco: An Environmental Pilot Study on Oahu, Hawaii, USA. Journal of Geoscience and Environment Protection, 8, 130-139. https://doi.org/10.4236/gep.2020.86010.

Hsiung, K. H., T. Kanamatsu, K. Ikehara, K. Usami, C. S. Horng, N. Ohkouchi, N. O. Ogawa, S. Saito, and M. Murayama (2021), X-ray fluorescence core scanning, magnetic signatures, and organic geochemistry analyses of Ryukyu Trench sediments: turbidites and hemipelagites, Progress in Earth and Planetary Science, 8(1), doi:10.1186/s40645-020-00396-2.

Kang, S. G., X. L. Wang, H. M. Roberts, G. A. T. Duller, Y. G. Song, W. G. Liu, R. Zhang, X. X. Liu, and J. H. Lan (2020), Increasing effective moisture during the Holocene in the semiarid regions of the Yili Basin, Central Asia: Evidence from loess sections, Quaternary Science Reviews, 246, doi:10.1016/j.quascirev.2020.106553.

Kapper, K. L., F. Bautista, A. Goguitchaishvili, M. F. Bogalo, R. Cejudo-Ruiz, and M. Cervantes Solano (2020), The use and misuse of magnetic methods to monitor environmental pollution in urban areas, Boletin De La Sociedad Geologica Mexicana, 72(1), doi:10.18268/BSGM2020v72n1a111219.

Karampaglidis, T., A. Benito-Calvo, A. Rodes, R. Braucher, A. Perez-Gonzalez, J. Pares, F. Stuart, L. Di Nicola, and D. Bourles (2020), Pliocene endorheic-exhoreic drainage transition of the Cenozoic Madrid Basin (Central Spain), Global and Planetary Change, 194, doi:10.1016/j.gloplacha.2020.103295.

Kumar, C. K. S., and A. Chandrasekaran (2020), Multivariate statistical tool to analyse the environmental magnetic data in Ponnai River Sand, Tamil Nadu, Environmental Earth Sciences, 79(21), doi:10.1007/s12665-020-09241-7.

Li, J. H., N. Menguy, E. Leroy, A. P. Roberts, P. Y. Liu, and Y. X. Pan (2020c), Biomineralization and Magnetism of Uncultured Magnetotactic Coccus Strain THC-1 With Non-chained Magnetosomal Magnetite Nanoparticles, Journal of Geophysical Research-Solid Earth, 125(12), doi:10.1029/2020jb020853.

Li, J. H., P. Y. Liu, J. Wang, A. P. Roberts, and Y. X. Pan (2020a), Magnetotaxis as an Adaptation to Enable Bacterial Shuttling of Microbial Sulfur and Sulfur Cycling Across Aquatic Oxic-Anoxic Interfaces, Journal of Geophysical Research-Biogeosciences, 125(12), doi:10.1029/2020jg006012.

Li, J. H., Y. Liu, S. C. Liu, A. P. Roberts, H. M. Pan, T. A. Xiao, and Y. X. Pan (2020b), Classification of a Complexly Mixed Magnetic Mineral Assemblage in Pacific Ocean Surface Sediment by Electron Microscopy and Supervised Magnetic Unmixing, Frontiers in Earth Science, 8, doi:10.3389/feart.2020.609058.

Liu, H. J., Q. X. Liu, J. Q. Chen, and D. L. Zhang (2020), Study of the recent sediment movement features in the vicinity of Deepwater Navigation Channel, Yangtze estuary, Estuarine Coastal and Shelf Science, 245, doi:10.1016/j.ecss.2020.106993.

Lopez-Perez, A. E., B. Rubio, D. Rey, M. Plaza-Morlote, and L. M. Pinheiro (2021), Late Quaternary tectono-sedimentary processes on an isolated offshore high marginal platform (NW Iberian Continental Margin), Marine Geology, 431, doi:10.1016/j.margeo.2020.106374.

Miao, X. M., X. L. Feng, J. R. Li, and L. Lin (2021), Tracing the paleo-methane seepage activity over the past 20,000 years in the sediments of Qiongdongnan Basin, northwestern South China Sea, Chemical Geology, 559, doi:10.1016/j.chemgeo.2020.119956.

Njau, J. K., N. Toth, K. Schick, I. G. Stanistreet, L. J. McHenry, and H. Stollhofen (2021), The Olduvai Gorge Coring Project: Drilling high resolution palaeoclimatic and palaeoenvironmental archives to constrain hominin evolution, Palaeogeography Palaeoclimatology Palaeoecology, 561, doi:10.1016/j.palaeo.2020.110059.

Oudeika, M. S., F. F. Altinoglu, F. Akbay, and A. Aydin (2020), The use of magnetic susceptibility and chemical analysis data for characterizing heavy metal contamination of topsoil in Denizli city, Turkey, Journal of Applied Geophysics, 183, doi:10.1016/j.jappgeo.2020.104208.

Ouyang, T. P., M. K. Li, Y. Guo, S. S. Peng, C. J. He, and Z. Y. Zhu (2020), Magnetic Difference Between Deep and Surface Soil Within an Agricultural Area in Southern China: Implications for Magnetic Mineral Transformation During Pedogenic Process Under Subtropical Climate, Earth and Space Science, 7(10), doi:10.1029/2019ea001070.

Qian, Y., A. P. Roberts, Y. Liu, P. X. Hu, X. Zhao, D. Heslop, K. M. Grant, E. J. Rohling, R. Hennekam, and J. H. Li (2020), Assessment and Integration of Bulk and Component-Specific Methods for Identifying Mineral Magnetic Assemblages in Environmental Magnetism, Journal of Geophysical Research-Solid Earth, 125(8), doi:10.1029/2019jb019024.

Ramon, R., O. Evrard, J. P. Laceby, L. Caner, A. V. Inda, C. A. P. de Barros, J. P. G. Minella, and T. Tiecher (2020), Combining spectroscopy and magnetism with geochemical tracers to improve the discrimination of sediment sources in a homogeneous subtropical catchment, Catena, 195, doi:10.1016/j.catena.2020.104800.

Reilly, B. T., M. L. McCormick, S. A. Brachfeld, and B. A. Haley (2020), Authigenic Ferrimagnetic Iron Sulfide Preservation Due to Nonsteady State Diagenesis: A Perspective From Perseverance Drift, Northwestern Weddell Sea, Geochemistry Geophysics Geosystems, 21(11), doi:10.1029/2020gc009380.

Ren, J., X. Y. Long, J. F. Ji, V. Barron, J. Torrent, Y. Wang,

and S. Y. Xie (2020), Different Enrichment Patterns of Magnetic Particles Modulated by Primary Iron-Phosphorous Input, Geophysical Research Letters, 47(22), doi:10.1029/2020gl090439.

Reolid, M., J. Iwanczuk, E. Mattioli, and I. Abad (2020), Integration of gamma ray spectrometry, magnetic susceptibility and calcareous nannofossils for interpreting environmental perturbations: An example from the Jenkyns Event (lower Toarcian) from South Iberian Palaeomargin (Median Subbetic, SE Spain), Palaeogeography Palaeoclimatology Palaeoecology, 560, doi:10.1016/j.palaeo.2020.110031.

Senouci, M., and K. Allek (2020), Application of Bayesian classifier to magnetic and gamma ray spectrometry data for targeting hydrocarbon microseepages, Journal of Applied Geophysics, 181, doi:10.1016/j.jappgeo.2020.104145.

Tan, M. Q., W. L. Zhang, X. M. Fang, M. D. Yan, J. B. Zan, and T. Zhang (2020), Rock magnetic record of core SG-3 since 1 Ma in the western Qaidam Basin and its paleoclimate implications for the NE Tibetan Plateau, Palaeogeography Palaeoclimatology Palaeoecology, 560, doi:10.1016/j.palaeo.2020.109949.

Wang, S., J. Liu, J. C. Li, L. Xu, G. Xu, Y. S. Jiang, X. Zhang, H. X. Wang, and J. D. Qiu (2020), Environmental magnetic properties used to assess sediment sources and transport patterns in the muddy area along the Zhejiang coast, China, Estuarine Coastal and Shelf Science, 245, doi:10.1016/j.ecss.2020.106933.

Wang, Z. X., Z. Zhang, C. J. Huang, J. M. Shen, Y. Sui, and Z. Q. Qian (2021), Astronomical forcing of lake evolution in the Lanzhou Basin during early Miocene period, Earth and Planetary Science Letters, 554, doi:10.1016/j.epsl.2020.116648.

Yamazaki, T. (2020), Reductive dissolution of biogenic magnetite, Earth Planets and Space, 72(1), doi:10.1186/s40623-020-01290-3.

Yang, H., et al. (2020), Loess depositional dynamics and paleoclimatic changes in the Yili Basin, Central Asia, over the past 250 ka, Catena, 195, doi:10.1016/j.catena.2020.104881.

Zhang, T., W. X. Han, X. M. Fang, C. H. Song, Y. D. Wang, Q. Tian, W. L. Zhang, Z. T. Feng, and M. Q. Tan (2021), Tectonic forcing of environmental transition in Central Asia at-11-9 Ma, Gondwana Research, 89, 19-30.

Zhang, Z. L., J. M. Sun, L. X. Lu, S. C. Tian, and M. M. Cao (2020), Neogene climate evolution of the Tarim Basin, NW China: Evidence from environmental magnetism of the southern Tian Shan foreland, Global and Planetary Change, 194, doi:10.1016/j.gloplacha.2020.103314.

Zhao, G. Y., Y. Han, X. M. Liu, B. Lu, Q. Chen, R. L. Zhang, J. M. Ma, H. M. Li, and J. B. Zhao (2020), Causation and mechanism of magnetic susceptibility trend in Upper Miocene-Pliocene red clay deposits of the eastern Chinese Loess Plateau, Palaeogeography Palaeoclimatology Palaeoecology, 560, doi:10.1016/j.palaeo.2020.110014.

Extraterrestrial and Planetary Magnetism

Bischoff, A., et al. (2021), The old, unique C1 chondrite Flensburg - Insight into the first processes of aqueous alteration, brecciation, and the diversity of water-bearing parent bodies and lithologies, Geochimica Et Cosmochimica Acta, 293, 142-186, doi:10.1016/j.gca.2020.10.014.

Horgan, B. H. N., et al. (2020), Diagenesis of Vera Rubin Ridge, Gale Crater, Mars, From Mastcam Multispectral Images, Journal of Geophysical Research-Planets, 125(11), doi:10.1029/2019je006322.

Jacob, S. R., et al. (2020), Spectral, Compositional, and Physical Properties of the Upper Murray Formation and Vera Rubin Ridge, Gale Crater, Mars, Journal of Geophysical Research-Planets, 125(11), doi:10.1029/2019je006290.

L'Haridon, J., et al. (2020), Iron Mobility During Diagenesis at Vera Rubin Ridge, Gale Crater, Mars, Journal of Geophysical Research-Planets, 125(11), doi:10.1029/2019je006299.

Lindgren, P., et al. (2020), Signatures of the post-hydration heating of highly aqueously altered CM carbonaceous chondrites and implications for interpreting asteroid sample returns, Geochimica Et Cosmochimica Acta, 289, 69-92, doi:10.1016/j.gca.2020.08.021.

Liu, T. X., Z. F. Bai, and Y. Zhao (2020), Research on the retention characteristics of the stratification information of lunar soil drilling sampling, Advances in Space Research, 66(10), 2428-2445, doi:10.1016/j.asr.2020.08.002.

Fraeman, A. A., et al. (2020), Evidence for a Diagenetic Origin of Vera Rubin Ridge, Gale Crater, Mars: Summary and Synthesis of Curiosity's Exploration Campaign, Journal of Geophysical Research-Planets, 125(12), doi:10.1029/2020je006527.

Maxwell, R. E., and I. Garrick-Bethell (2020), Evidence for an Ancient Near-Equatorial Lunar Dipole From Higher Precision Inversions of Crustal Magnetization, Journal of Geophysical Research-Planets, 125(12), doi:10.1029/2020je006567.

Fundamental Rock Magnetism and direct Applications

Abdelmalak, M. M., and S. Polteau (2020), The thermal maturity of sedimentary basins as revealed by magnetic mineralogy, Basin Research, 32(6), 1510-1531, doi:10.1111/bre.12439.

Belokon, V. I., and O. I. Dyachenko (2020), Long- and Short-Range Magnetic Order in Titanomagnetite, Izvestiya-Physics of the Solid Earth, 56(6), 888-891, doi:10.1134/s1069351320060014.

Hodel, F., M. Macouin, R. I. F. Trindade, J. Araujo, M. Respaud, J. F. Meunier, L. Cassayre, S. Rousse, L. Drigo, and J. Schorne-Pinto (2020), Magnetic Properties of Ferritchromite and Cr-Magnetite and Monitoring of Cr-Spinels Alteration in Ultramafic and Mafic Rocks, Geochemistry Geophysics Geosystems, 21(11), doi:10.1029/2020gc009227.

Li, Z. Y., Q. Xiong, and J. P. Zheng (2020), Magnetic Signature of Serpentinization at Zedang in the South Tibetan Ophiolite Belt, Acta Geologica Sinica-English Edition, 94, 28-28, doi:10.1111/1755-6724.14443.

Lied, P., Kontny, A., Nowaczyk, N., Mrlina, J., and H. Kämpf (2020), Cooling rates of pyroclastic deposits inferred from mineral magnetic investigations: a case study from the Pleistocene Mýtina Maar (Czech Republic), International Journal of Earth Sciences, https://doi.org/10.1007/s00531-020-01865-1.

Nikolaisen, E. S., R. J. Harrison, K. Fabian, and S. A. McEnroe (2020), Hysteresis of Natural Magnetite Ensembles: Micromagnetics of Silicate-Hosted Magnetite Inclusions Based on Focused-Ion-Beam Nanotomography, Geochemistry Geophysics Geosystems, 21(11), doi:10.1029/2020gc009389.

Yang, T., Y. M. Chou, E. C. Ferre, M. J. Dekkers, J. Y. Chen, E. C. Yeh, and W. Tanikawa (2020), Faulting Processes Unveiled by Magnetic Properties of Fault Rocks, Reviews of Geophysics, 58(4), doi:10.1029/2019rg000690.

Geomagnetism, Paleointensity and Records of the Geomagnetic Field

Calvo-Rathert, M., B.galo, M. F., Morales, J., Goguitchaichvili, A., Lebedev, V. A., Vashakidze, G., et al. (2021), An integrated paleomagnetic, multimethod-paleointensity, and radiometric study on Cretaceous and Paleogene lavas from the Lesser Caucasus: Geomagnetic and tectonic implica-

tions. Journal of Geophysical Research: Solid Earth, 126, e2020JB020019. https://doi.org/10.1029/2020JB020019.

Cervantes-Solano, M., A. Goguitchaichvili, L. S. Bettucci, J. Morales-Contreras, C. Gogorza, and P. Nunez (2020a), An integrated paleomagnetic and multispecimen paleointensity study from the late Jurassic Zapican dike swarm (Uruguay), Journal of South American Earth Sciences, 104, doi:10.1016/j.jsames.2020.102815.

Herrero-Bervera, E., and I. Snowball (2020), Integrated high-resolution PSV, RPI and 14C study of IODP-347 Site M0060 (Anholt Loch, Baltic Sea) for the last c. 14 ka, in: Tema, E., Di Chiara, A., and E. Herrero-Bervera (eds) Geomagnetic Field Variations in the Past: New Data, Applications and Recent Advances. Geological Society, London, Special Publications, 497, https://doi.org/10.1144/SP497-2019-147.

Huder, L., N. Gillet, C. C. Finlay, M. D. Hammer, and H. Tchoungui (2020), COV-OBS.x2: 180 years of geomagnetic field evolution from ground-based and satellite observations, Earth Planets and Space, 72(1), doi:10.1186/s40623-020-01194-2.

Liu, J. B., N. R. Nowaczyk, S. Panovska, M. Korte, and H. W. Arz (2020), The Norwegian-Greenland Sea, the Laschamps, and the Mono Lake Excursions Recorded in a Black Sea Sedimentary Sequence Spanning From 68.9 to 14.5 ka, Journal of Geophysical Research-Solid Earth, 125(8), doi:10.1029/2019jb019225.

Mauerberger, S., M. Schanner, M. Korte, and M. Holschneider (2020), Correlation based snapshot models of the archeomagnetic field, Geophysical Journal International, 223(1), 648-665, doi:10.1093/gji/ggaa336.

Instruments and Techniques

Qin, H. F., X. Zhao, S. C. Liu, G. A. Paterson, Z. X. Jiang, S. H. Cai, J. H. Li, Q. S. Liu, and R. X. Zhu (2020), An ultra-low magnetic field thermal demagnetizer for high-precision paleomagnetism, Earth Planets and Space, 72(1), doi:10.1186/s40623-020-01304-0.

Ribeiro, N., R. Bijani, and C. Ponte-Neto (2020), Improving the crosscorrelation method to estimate the total magnetization direction vector of isolated sources: A space-domain approach for unstable inclination values, Geophysics, 85(4), J59-J70, doi:10.1190/geo2019-0008.1.

Liu, S., X. Y. Hu, D. L. Zhang, B. S. Wei, M. X. Geng, B. X. Zuo, H. L. Zhang, and S. Vatankhah (2020), The IDQ curve: A tool for evaluating the direction of remanent magnetization from magnetic anomalies, Geophysics, 85(5), J85-J98, doi:10.1190/geo2019-0545.1.

Magnetic Fabrics and Anisotropy

Archanjo, C. J. (2020), Composite magmatic/magnetic fabrics evidences late AMS in syn-tectonic dikes in the Monteiro-Sume plutonic-volcanic complex (NE Brazil), Journal of Structural Geology, 140, doi:10.1016/j.jsg.2020.104154.

Austin, J. R., and B. O. Patterson (2020), Deciphering deformation in ultramafic intrusions via magnetic fabric (AMS) and palaeomagnetic studies, Savannah Ni-PGE camp, NW Australia, Tectonophysics, 793, doi:10.1016/j.tecto.2020.228608.

Avila, C. F., C. J. Archanjo, M. Hollanda, A. A. de Macedo, and D. D. Lemos-Santos (2020), Shear zone cooling and fabrics of synkinematic plutons evidence timing and rates of orogenic exhumation in the northwest Borborema Province (NE Brazil), Precambrian Research, 350, doi:10.1016/j.precamres.2020.105940.

Biedermann, A. R. (2020), Current challenges and future developments in magnetic fabric research, Tectonophysics, 795, doi:10.1016/j.ieeto.2020.228632.

Biedermann, A. R. (2020), FinIrrSDA: A 3-D Model for Magnetic Shape and Distribution Anisotropy of Finite Irregular Arrangements of Particles With Different Sizes, Geometries, and Orientations, Journal of Geophysical Research-Solid Earth, 125(12), doi:10.1029/2020jb020300.

Biedermann, A. R., M. Jackson, M. Chadima, A. M. Hirt, and J. M. Feinberg (2020), Beyond the second-order magnetic anisotropy tensor: higher-order components due to oriented magnetite exsolutions in pyroxenes, and implications for palaeomagnetic and structural interpretations, Geophysical Journal International, 223(2), 915-933, doi:10.1093/gji/ggaa355.

Bradak, B., Y. Seto, M. Chadima, J. Kovacs, P. Tanos, G. Ujvari, and M. Hyodo (2020), Magnetic fabric of loess and its significance in Pleistocene environment reconstructions, Earth-Science Reviews, 210, doi:10.1016/j.earscirev.2020.103385.

Cerny, J., R. Melichar, D. Vsiansky, and J. Drahokoupil (2020), Magnetic Anisotropy of Rocks: A New Classification of Inverse Magnetic Fabrics to Help Geological Interpretations, Journal of Geophysical Research-Solid Earth, 125(11), doi:10.1029/2020jb020426.

Chatue, C. N., T. Njanko, E. M. Fozing, B. E. B. Nke, N. Seta, and E. Njonfang (2020), Field observations, magnetic fabrics and microstructures evidences of syn-kinematic emplacement of the Numba granitic pluton (western Cameroon domain), Journal of African Earth Sciences, 172, doi:10.1016/j.jafrearsci.2020.104009.

Chou, Y. M., C. Aubourg, E. C. Yeh, S. R. Song, Y. K. Lin, F. Humbert, X. D. Jiang, and T. Q. Lee (2020), The Magnetic Fabric of Gouge Mimics the Coseismic Focal Mechanism of the Chi-Chi Earthquake (1999, Mw 7.6), Geophysical Research Letters, 47(22), doi:10.1029/2020gl090111.

Ejembi, J. I., E. C. Ferre, S. Satolli, and S. A. Friedman (2020), Post-Depositional Fluid Flow in Jurassic Sandstones of the Uncompahgre Uplift: Insights From Magnetic Fabrics, Frontiers in Earth Science, 8, doi:10.3389/feart.2020.601415.

Katiyar, V., S. K. Patil, and H. B. Srivastava (2020), New Magnetic Fabric Data from Almora Crystalline Rocks around Rameshwar, Near North Almora Thrust, Journal of the Geological Society of India, 96(4), 349-355, doi:10.1007/s12594-020-1563-4.

Li, J. X., Z. W. Li, S. G. Liu, K. Tong, Y. H. Ye, B. Ran, and C. Han (2020), Magnetic fabrics of the South Dabashan Belt at the north margin of South China: Constraint on the origin of the arcuate trace of Chengkou Fault, Journal of Structural Geology, 140, doi:10.1016/j.jsg.2020.104149.

Merabet, N. E., B. Henry, S. Maouche, A. Abtout, Y. Mahdjoub, A. Lamali, and M. Ayache (2020), Paleoproterozoic structural evolution of the Eglab domain (Eglab shield, Algeria) from aeromagnetic data and anisotropy of magnetic susceptibility (AMS) study of the post-collisional Aftout granitoids, Journal of African Earth Sciences, 172, doi:10.1016/j.jafrearsci.2020.103979.

Moreno, E., et al. (2020), Magnetic fabric of Bengal fan sediments: Holocene record of sedimentary processes and turbidite activity from the Ganges-Brahmaputra river system, Marine Geology, 430, doi:10.1016/j.margeo.2020.106347.

Pares, J. M., I. Campana, M. Duval, M. J. Sier, A. I. Ortega, G. I. Lopez, and J. Rosell (2020), Comparing depositional modes of cave sediments using magnetic anisotropy, Journal of Archaeological Science, 123, doi:10.1016/j.jas.2020.105241.

Pasqualon, N. G., J. F. Savian, E. F. Lima, F. R. Luz, T. R. Moncinhatto, and R. I. F. Trindade (2020), Emplacement

dynamics of alkaline volcanic and subvolcanic rocks in Trindade Island, Brazil, Journal of Volcanology and Geothermal Research, 406, doi:10.1016/j.jvolgeores.2020.107078.

Trippanera, D., M. Porreca, S. Urbani, C. Kissel, A. Winkler, L. Sagnotti, S. Nazzareni, and V. Acocella (2020), Interpreting Inverse Magnetic Fabric in Miocene Dikes From Eastern Iceland, Journal of Geophysical Research-Solid Earth, 125(11), doi:10.1029/2020jb020306.

Xian, F., and R. Zhang (2020), An Attempt to Recover a Paleomonsoon Signal in the Chinese Loess Plateau Using Anisotropy of Magnetic Susceptibility, Frontiers in Earth Science, 8, doi:10.3389/feart.2020.569072.

Mineral Physics, Chemistry, Mineralogy and Petrology

Bylaska, E. J., D. Song, and K. M. Rosso (2020), Electron transfer calculations between edge sharing octahedra in hematite, goethite, and annite, Geochimica Et Cosmochimica Acta, 291, 79-91, doi:10.1016/j.gca.2020.04.036.

Canton, L. C., I. G. de Souza, L. S. Silva, M. Marques, and A. C. S. da Costa (2021), Identification and quantification of iron oxides by diffuse reflectance spectroscopy with Praying Mantis accessory and integration sphere, Catena, 196, doi:10.1016/j.catena.2020.104899.

Chen, C. M., and A. Thompson (2021), The influence of native soil organic matter and minerals on ferrous iron oxidation, Geochimica Et Cosmochimica Acta, 292, 254-270, doi:10.1016/j.gca.2020.10.002.

Jin, L., et al. (2021), Atomic-scale characterization of commensurate and incommensurate vacancy superstructures in natural pyrrhotites, American Mineralogist, 106(1), 82-96, doi:10.2138/am-2020-7479CCBY.

Liu, C. S., M. S. Massey, D. E. Latta, Y. F. Xia, F. B. Li, T. Gao, and J. Hua (2021), Fe(II)-induced transformation of iron minerals in soil ferromanganese nodules, Chemical Geology, 559, doi:10.1016/j.chemgeo.2020.119901.

Nienhuis, E. T., J. Marcial, T. Robine, C. Le Losq, D. R. Neuville, M. C. Stennett, N. C. Hyatt, and J. S. McCloy (2020), Effect of Ti4+ on the structure of nepheline (NaAlSiO4) glass, Geochimica Et Cosmochimica Acta, 290, 333-351, doi:10.1016/j.gca.2020.09.015.

Salazar, J. R., D. J. Pfotenhauer, F. Leresche, F. L. Rosario-Ortiz, M. P. Hannigan, S. C. Fakra, and B. J. Majestic (2020), Iron Speciation in PM2.5 From Urban, Agriculture, and Mixed Environments in Colorado, USA, Earth and Space Science, 7(10), doi:10.1029/2020ea001262.

Yu, Y., and B. Tikoff (2020), Magnetic Cr-Rich Spinel in Serpentinized Ultramafic Complexes, Journal of Geophysical Research-Solid Earth, 125(11), doi:10.1029/2020jb020443.

Paleomagnetism

Abu El-Ela, F. F., A. N. Mahgoub, H. A. Ibrahim, I. A. El-Hemaly, L. M. Alva-Valdivia, and H. Bohnel (2020), Paleomagnetism of a late Neoproterozoic mafic-ultramafic layered intrusion of Gebel Dahanib, South Eastern Desert (Egypt): Implications for magma evolution and timing of magnetization acquisition, Journal of African Earth Sciences, 172, doi:10.1016/j.jafrearsci.2020.104016.

Cao, Y., Z. M. Sun, H. B. Li, X. W. Cao, C. G. Liu, X. Z. Ye, C. L. Li, and L. Zhang (2020), Paleomagnetic study of the Late Cretaceous red beds in the eastern segement of the Bangong-Nujiang suture zone and its tectonic implications, Acta Petrologica Sinica, 36(10), 3243-3255, doi:10.18654/1000-0569/2020.10.18.

Cervantes-Solano, M. A., U. D. Ortega, A. Goguitchaichvili, J. Rosas-Elguera, J. M. Contreras, R. Garcia-Ruiz, and R. Cejudo-Ruiz (2020b), Paleomagnetic study from radiometrically dated lavas associated to the Tepic-Zacoalco Rift (western Mexico): Possible evidence of a new geomagnetic excursion within Gilbert chron, Journal of South American Earth Sciences, 104, doi:10.1016/j.jsames.2020.102796.

Dallanave, E., and U. Kirscher (2020), Testing the Reliability of Sedimentary Paleomagnetic Datasets for Paleogeographic Reconstructions, Frontiers in Earth Science, 8, doi:10.3389/feart.2020.592277.

Fazzito, S. Y., A. E. Rapalini, S. E. Geuna, and D. G. Poire (2020), Remagnetized limestones and dolostones from the Upper Cambrian La Flecha Formation, La Rioja province, Argentine Precordillera, Journal of South American Earth Sciences, 104, doi:10.1016/j.jsames.2020.102891.

Hansma, J., and E. Tohver (2020), Southward Drift of Eastern Australian Hotspots in the Paleomagnetic Reference Frame Is Consistent With Global True Polar Wander Estimates, Frontiers in Earth Science, 8, doi:10.3389/feart.2020.544496.

Huang, W. T., M. J. Jackson, M. J. Dekkers, P. Solheid, Y. Zhang, S. H. Li, Z. J. Guo, and L. Ding (2020), Remagnetization of Red Beds on the Tibetan Plateau: Mechanism and Diagnosis, Journal of Geophysical Research-Solid Earth, 125(8), doi:10.1029/2020jb020068.

Katagiri, T., H. Naruse, N. Ishikawa, and T. Hirata (2020), Collisional bending of the western Paleo-Kuril Arc deduced from paleomagnetic analysis and U-Pb age determination, Island Arc, 29(1), doi:10.1111/iar.12329.

Marton, E., J. Madzin, D. Plasienka, J. Grabowski, J. Bucova, R. Aubrecht, and M. Putis (2020), New paleomagnetic constraints for the large-scale displacement of the Hronic nappe system of the Central Western Carpathians, Journal of Geodynamics, 141, doi:10.1016/j.jog.2020.101796.

Metelkin, D. V., A. I. Chernova, N. Y. Matushkin, and V. A. Vernikovsky (2020), Paleozoic Tectonics and Geodynamics of the De Long Islands and Adjacent Structures of the Verkhoyansk-Chukotka Fold Belt, Doklady Earth Sciences, 495(1), 803-807, doi:10.1134/s1028334x20110100.

Molina-Garza, R. S., J. Pindell, and P. C. M. Cortes (2020), Slab flattening and tractional coupling drove Neogene clockwise rotation of Chiapas Massif, Mexico: Paleomagnetism of the Eocene El Bosque Formation, Journal of South American Earth Sciences, 104, doi:10.1016/j.jsames.2020.102932.

Oriolo, S., B. Schulz, S. Geuna, P. D. Gonzalez, J. E. Otamendi, J. Slama, E. Druguet, and S. Siegesmund (2021), Early Paleozoic accretionary orogens along the Western Gondwana margin, Geoscience Frontiers, 12(1), 109-130, doi:10.1016/j.gsf.2020.07.001.

Otofuji, Y., M. Fujihara, and K. Uno (2021), Chronology of serpentinization: Paleomagnetic evidence for 20 Ma serpentinization of the Oeyama ophiolite, Wakasa, Southwest Japan, Earth and Planetary Science Letters, 554, doi:10.1016/j.epsl.2020.116656.

Pasenko, A. M., and S. V. Malyshev (2020), Paleomagnetism and Age Correlation of the Mesoproterozoic Rocks of the Udzha and Olenek Uplifts, Northeastern Siberian Platform, Izvestiya-Physics of the Solid Earth, 56(6), 864-887, doi:10.1134/s1069351320050067.

Peng, Y. B., S. Y. Yu, S. Z. Li, Y. J. Liu, M. Santosh, P. Lv, Y. S. Li, W. M. Xie, and Y. M. Liu (2020), The odyssey of Tibetan Plateau accretion prior to Cenozoic India-Asia collision: Probing the Mesozoic tectonic evolution of the Bangong-Nujiang Suture, Earth-Science Reviews, 211, doi:10.1016/j.earscirev.2020.103376.

Shatsillo, A. V., S. V. Rud'ko, I. V. Latysheva, D. V. Rud'ko, I. V. Fedyukin, V. I. Powerman, and N. B. Kuznetsov (2020), A Devious Equatorial Dipole Hypothesis: on the Low-Latitude Glaciations Problem and Geomagnetic Field Configu-

ration in Late Precambrian, Izvestiya-Physics of the Solid Earth, 56(6), 833-853, doi:10.1134/s1069351320060087.
Venkateshwarlu, M. (2020), New paleomagnetic pole and magnetostratigraphy of the Cauvery Basin sediments, southern India, Journal of Earth System Science, 129(1), doi:10.1007/s12040-020-01476-z.
Wen, B., D. A. D. Evans, R. P. Anderson, and P. J. A. McCausland (2020), Late Ediacaran paleogeography of Avalonia and the Cambrian assembly of West Gondwana, Earth and Planetary Science Letters, 552, doi:10.1016/j.epsl.2020.116591.
Westerweel, J., A. Licht, N. Cogne, P. Roperch, G. Dupont-Nivet, M. K. Thi, H. H. Swe, H. S. Huang, Z. Win, and D. W. Aung (2020), Burma Terrane Collision and Northward Indentation in the Eastern Himalayas Recorded in the Eocene-Miocene Chindwin Basin (Myanmar), Tectonics, 39(10), doi:10.1029/2020tc006413.
Zhang, Y., et al. (2020), Fluid Migration and Widespread Remagnetization in the Dabashan Fold and Thrust Belt, China, Journal of Geophysical Research-Solid Earth, 125(11), doi:10.1029/2020jb019989.

Stratigraphy

Baraboshkin, E. Y., A. Y. Guzhikov, G. N. Aleksandrova, V. A. Fomin, B. G. Pokrovsky, V. A. Grishchenko, A. G. Manikin, and E. V. Naumov (2020), New Sedimentological, Magnetostratigraphic, and Biostratigraphic Data on the Campanian-Maastrichtian of Beshkosh Mountain, Southwest Crimea, Stratigraphy and Geological Correlation, 28(8), 816-858, doi:10.1134/s0869593820060040.
Franceschinis, P. R., M. P. Escayola, A. E. Rapalini, and C. R. Piceda (2020), Age constraints on the Cambrian Meson Group (NW Argentina) based on detrital zircons U-Pb geochronology and magnetic polarity bias, Journal of South American Earth Sciences, 104, doi:10.1016/j.jsames.2020.102835.
Gibert, L., A. Deino, L. Valero, F. Anaya, M. Leria, B. Saylor, and D. A. Croft (2020), Chronology of Miocene terrestrial deposits and fossil vertebrates from Quebrada Honda (Bolivia), Palaeogeography Palaeoclimatology Palaeoecology, 560, doi:10.1016/j.palaeo.2020.110013.
Jovane, L., F. Florindo, G. Wilson, S. Leone, M. Bin Hassan, D. Rodelli, and G. Cortese (2020), Magnetostratigraphic Chronology of a Cenozoic Sequence From DSDP Site 274, Ross Sea, Antarctica, Frontiers in Earth Science, 8, doi:10.3389/feart.2020.563453.
Martinez, M., R. Aguado, M. Company, J. Sandoval, and L. O'Dogherty (2020), Integrated astrochronology of the Barremian Stage (Early Cretaceous) and its biostratigraphic subdivisions, Global and Planetary Change, 195, doi:10.1016/j.gloplacha.2020.103368.
Michalik, J., J. Grabowski, O. Lintnerova, D. Rehakova, S. Kdyr, and P. Schnabl (2021), Jurassic - Cretaceous boundary record in Carpathian sedimentary sequences, Cretaceous Research, 118, doi:10.1016/j.cretres.2020.104659.
Maron, M., and G. Muttoni (2021), A detailed record of the C34n/C33r magnetozone boundary for the definition of the base of the Campanian Stage at the Bottaccione section (Gubbio, Italy), Newsletters on Stratigraphy, 54(1), 107-122, doi:10.1127/nos/2020/0607.

cont'd. from pg. 1...

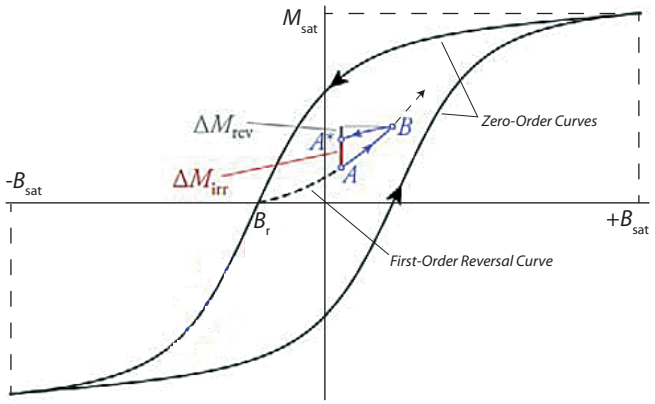

Figure 1. The major hysteresis loop (black lines with large arrows) is composed of two zero-order magnetization curves starting from positive and negative saturation, respectively. First-order magnetization curves originate from the major hysteresis if the field sweep is reversed before reaching negative saturation at a reversal field B_r and measuring the magnetization back to B_{sat} (dashed black line). For any discrete point on a magnetization curve (e.g. point A at the end of the dashed line), magnetization changes can be decomposed into a reversible (ΔM_{rev}) and an irreversible (ΔM_{irr}) component by sweeping the field a little further to point *B* and then back to the original field. Because of the irreversible component ΔM_{irr}, the resulting magnetization does not coincide with A, but is instead larger (point A*). Modified after Egli and Winklhofer (2014), see text for details.

curring in geologic materials. Individual magnetic particles might possess two or more pairs of magnetic states, depending on parameters such as size and shape. These so-called microstates contribute to the bulk magnetization of the specimen. Partial information on the magnetic particle assemblage is obtained by measuring the dependence of the bulk magnetization on the applied field and other parameters, such as temperature, according to specific measurement protocols (e.g., magnetic hysteresis, IRM acquisition curves, thermomagnetic curves). Because virtually infinite combinations of microstates can yield the same bulk magnetization, the interpretation of results obtained from such measurement protocols is intrinsically non-unique. FORC measurements reduce this non-uniqueness, without eliminating it, through a systematic scan of the transitions between microstates that contribute to the bulk hysteresis. With this scan, it is possible to visualize magnetization processes that are specific for certain domain states, and the magnetic interactions existing between particles, in a two-dimensional function known as the FORC diagram.

The FORC measurement protocol consists of partial hysteresis curves that originate from the same branch of the major loop, which is typically the descending branch. For reference, the branches of a hysteresis loop are also referred to as zero-order curves, because they originate directly from a saturated state (M_s) attained at a saturation field B_{sat}. Reversing the field at a given field-value B_r before (negative) saturation is reached ($-B_{sat}$), and measuring the magnetization from B_r back to $+B_{sat}$ in discrete field increments, allows accessing the inner area of the hysteresis loop by measuring an individual first-order reversal curve. When describing magnetization curves,

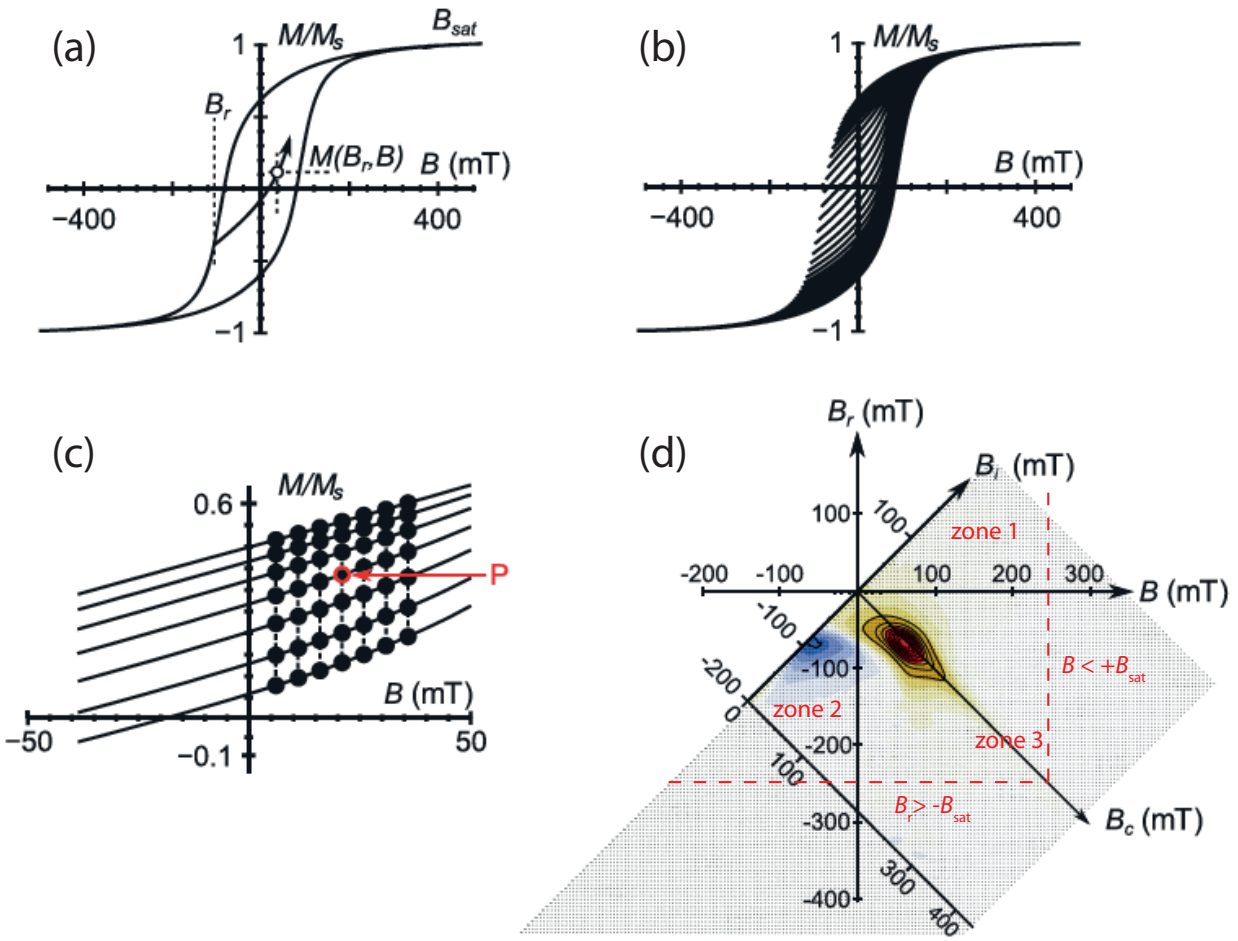

Figure 2. (a) First-Order Reversal Curve starting at B_r towards B_{sat}, with magnetization at each point B measurements along the FORC represented by $M(B_r, B)$; (c) FORC measurements for different increments of B_r allow accessing the inner area of the hysteresis loop (the outer envelope of the FORCs defines the major loop); (d) FORC distribution $\rho(B_r, B)$ calculated at a point P using measurements from consecutive FORCs for SF = 3 (smoothing is performed over $(2SF + 1)^2 = 7 \times 7$ about P; (e) FORC diagram showing the relationship between the $\{B_r, B\}$ and the $\{B_i, B_c\}$ coordinate systems. The FORC distribution is confined to the triangular region between the $B_i \geq B$ diagonal line and the red dashed lines $B_r > -B_{sat}$ and $B < +B_{sat}$, which can be further subdivided into zones 1, 2 where hysterons are positively or negatively saturated in zero field, and zone 3, where hysterons can have two magnetization states in zero field, and within wich remanent magnetizations originate. Modified after Roberts et al. (2014), see text for details.

an important distinction is made between magnetization changes due to reversible and irreversible processes, and become important to understanding the different contributions to FORC diagrams. The two types of processes occurring along any magnetization curve are discriminated by comparing a small portion $M_A \rightarrow M_B$ of the curve between close fields B_A and B_B with the magnetization M_{*A} obtained by sweeping the field from B_B back to B_A (Fig. 1). Because of magnetic hysteresis, $M_B \rightarrow M_{A*}$ does not follow the same path as $M_A \rightarrow M_B$, and therefore $M_{A*} \neq M_A$, the difference $M_{A*} - M_A$ is the irreversible magnetization change occurring when sweeping the field from B_A to B_B , while $M_B - M_{A*}$ is the reversible change. The sum of the two contributions equals $M_B - M_A$.

The magnetization at applied field B on the FORC with reversal point B_r is denoted by $M(B_r, B)$, where $B \geq B_r$ (Fig. 2a). Repeating the process for different equally spaced values (increment δB) of B_r, allows collecting a number of FORCs (Fig. 2b), composed of gridded discreet magnetization measurements (Fig. 2c) used to create a FORC diagram (Fig. 2d).

The FORC distribution function was first described by Hejda and Zelinka (1990) and is defined as the mixed second derivative:

$$\rho(B_r, B) = -\tfrac{1}{2}\, \partial^2 M(B_r, B) / (\partial B_r \partial B), \quad (1)$$

over $B \geq B_r$.

The second derivative is scaled by ½ because the magnetization switch from $+M_s$ to $-M_s$ has a magnitude of $2M_s$. Purely reversible magnetization components (e.g. dia-, para-, and superparamagnetic) do not exhibit hysteresis, so they will be eliminated by the mixed second derivative and will not contribute to a FORC distribution. When plotting a FORC distribution, it is convenient to change coordinates from (B_r, B) to

$$B_c = (B_r - B) / 2; \; B_i \text{ or } B_u = (B_r + B) / 2$$

The (B_c, B_u) coordinate system is motivated by the phenomenological Preisach theory, in which B_c and B_u (or B_i) correspond to the coercivity and the bias field, respectively, of elemental rectangular hysteresis loops called

hysterons by analogy with elementary particles (Preisach, 1935). This means that the FORC diagram of identical particles featuring a squared hysteresis loop with coercivity B_c, which is offset on the field axis by a bias field B_u (e.g., from magnetostatic interactions), is given by an isolated peak contribution with coordinates (B_c, B_u). A continuous function in the FORC space can thus be explained mathematically as the result of the superposition of many hysterons characterized by a distribution of B_c and B_u values. This is the Preisach-Néel model introduced by Néel (1958), with marginal distributions along the B_c and B_u axes of the FORC diagram representing the distributions of coercivities and interaction fields, respectively. This model provides a partial explanation for SD particles, which are individually described by curved hysteresis loops with two magnetization jumps similar to those of hysterons, but fails at explaining the properties of larger particles possessing more than two magnetic states (Dumas et al., 2007; Newell, 2005; Pike & Fernandez, 1999), for a more detailed explanation see Egli and Winklhofer (2014) and Egli (2021). In this case, B_c and B_u no longer coincide with the coercivity and the interaction field of individual particles and the FORC function is merely an empirical signature of transitions between magnetic states occurring over certain ranges of fields.

Before describing some of these signatures, it is useful to explain some fundamental concepts rooted in the Preisach theory of hysteresis. Because the measurement protocol imposes that $B \geq B_r$, the FORC space is characterized by the half-plane $B_c \geq 0$ (Fig. 2d). This half-plane is further subdivided into three zones. The square defined by $B_r < 0$ and $B > 0$ is called the memory region (zone 3), because hysterons in this region can have two magnetization states in zero field. This means that all transitions between remanent magnetization states are recorded in this region only. This is therefore the most relevant region for the characterization of remanence carriers in paleomagnetic studies. The two triangles sandwiched between B_c=0 and the memory region constitute the so-called transient region, where hysterons are always in a positive, zone 1, or negative, zone 2, saturation state. As discussed above, hysterons are a fictive mathematical construct, and real magnetic particles can contribute to all three regions at the same time with different types of transitions between their magnetic states. Even SD particles contribute to the transient region in the lower quadrant ($B_u < 0$), due to the reversible rotation of magnetic moments while the field is swept from B_r to positive saturation (Newell, 2005).

Because of the definition of the FORC function as mixed derivative of the measured magnetization, integrals of the FORC function over specific domains, such as the memory region, yield magnetizations that can be compared with traditional rock magnetic parameters such as the saturation remanence M_{rs} (for the memory region), and the saturation magnetization M_s (for the whole FORC space). Moreover, well-known measurement protocols, such as DC demagnetization, and the irreversible component of the major hysteresis loop, coincide with subsets of the FORC measurement protocol, providing a quantitative link between FORC diagrams and common rock magnetic parameters, as well as different types of coercivity distribution (Egli, 2021).

Measuring and processing FORCs

The complexity of the FORC measurement protocol, the existence of special signatures such as the central ridge requiring high resolution, and the usually low signal-to-noise ratio resulting from the measurement of most natural samples, requires forward planning of FORC measurements and specific processing tools that have been developed recently. The close relationship existing between FORC diagrams and other magnetic parameters is an essential tool for interpreting complex mixtures of particle populations of the same mineral, or different minerals, and it is also essential for setting the correct measurement parameters of the FORC protocol. Measurement parameters, such as field ranges and resolution, will depend on the FORC features to be resolved and on the magnetic mineralogy. Direct calculation of the mixed second derivative amplifies measurement noise, which usually overwhelms the measured signal, therefore the data are smoothed over a suitable range of data points using an appropriate smoothing factor (SF) that will not degrade the signal. Different smoothing strategies have been developed, from polynomial fitting over squared point arrays (Pike et al., 1999), to polynomial fitting over arbitrary regions (FORCinel; Harrison & Feinberg, 2008), whose extension can be chosen to be field-dependent for optimal noise suppression (VARIFORC; Egli, 2013). Alternate, faster methods for preprocessing, which are based on the Fourier transform, have also been developed (Berndt & Chang, 2019). With these methods, the FORC function (equation 1) is evaluated on a grid within the boundaries of the FORC diagram, which are determined by the minimum and maximum measurement fields. Data are then contoured or plotted using a continuously varying color map that represents the FORC distribution (e.g. Fig. 2d). Modern processing algorithms also provide an error estimate, which can be used to highlight only those regions of the FORC space where the FORC function is significantly different from zero (Heslop & Roberts, 2012), avoiding overinterpretation issues. Moreover, measurement and processing of FORC diagrams have expanded to enable the separation of the FORC signal into the remanent (remFORCs), induced (iFORCs) and transient (tFORCs) components (Zhao et al., 2017). Here, only the classic FORC protocol is discussed.

Most of the early FORC literature revolves around uniaxial particles, with a particular focus on single domain (SD) grains owing to their importance as magnetic recorders. To correctly resolve their FORC signatures, (e.g., the "SD central ridge"), suitable measurement parameters must be chosen: Good FORC diagrams start with the correct choice of the extension of the FORC space, and the resolution with which the space is covered. The FORC space is controlled by the field ranges of the horizontal axis (from $B_c = 0$ to $B_c = B_{cmax}$) and of

Type	B_{cmax}	B_{umin} (filled space)	B_{umin} (VARIFORC)	B_{umax}	δB
Non-interacting SD	B_s	$-B_s$	$-0.1B_s$	$0.1B_s$	$\leq 0.01B_s$
Interacting SD	B_s	$-B_s$	$-0.1B_s$	$0.6B_s$	$\leq 0.02B_s$
Magnetofossil-bearing sediments	B_s (~120 mT)	$-0.7B_s$ (–80 mT)	$-0.1B_s$ (–10 mT)	$0.6B_s$ (+70 mT)	≤1 mT (0.5 mT)
PSD (generic, vortex)	B_s	$-B_s$	$-0.2B_s$	$+B_s$	$\leq 0.02B_s$
PSD (titano-)magnetite	~200 mT	–120 mT	–30 mT	+80 mT	1-2 mT
MD	$\sim 2B_{cr}$	$-B_s$	$-B_s + B_{cmax}$	$+B_s$	$<B_{c0}$

Table 1: Recommended FORC protocol parameters for different types of magnetic particles. B_s is the saturation field (i.e. the field amplitude at which the hysteresis loop becomes closed within the measurement uncertainty), B_{cr} is the coercivity of remanence, and B_{c0} the coercive field.

the vertical axis (from B_{umin} to B_{umax}). The FORC range is either chosen on the basis of a known magnetic mineralogy, or it is determined with the help of preliminary measurements such as the distribution of switching fields from the remanent hysteretic magnetization (M_{rh}) curve (e.g., Jackson & Solheid, 2010), or, more crudely, from the hysteresis loop and backfield curve. In the latter case, the relevant parameters are the coercivity of remanence, B_{cr}, and the saturation field B_s, defined as the field amplitude at which the two hysteresis branches merge within the uncertainty given by measurement errors. The merging point can be found visually by zooming on the loop. In the frequent case where high-coercivity contributions are present, a choice must be made to focus either on low-coercivity contributions (e.g., $B_{cmax} \approx 120$ mT) with a field resolution that is appropriate for this field range (δB = 0.5-2 mT), or on the maximum coercivity range enabled by the measuring instrument (in case of a VSM with electromagnet, $B_{cmax} \approx 1$ T without pole saturation correction) with a lower resolution that might be inadequate for the lower coercivity range (e.g. δB = 5-10 mT). For hard magnetic phases for which it is difficult, if not currently impossible, to achieve a saturated state with commonly available instruments, Roberts et al. (2006) argue that measurement of non-saturation properties can be adequate, and provide FORC diagrams for a range of hematite and goethite samples for this purpose.

The choice of the FORC range depends on B_s or B_{cr}, on the dominant domain state of the magnetic particles, and on the use of a FORC processing protocol capable of handling an incompletely filled FORC space, such as VARIFORC (Table 1). Handling of incompletely filled FORC space can save up to 50% measurement time, because the lower-left corner of the FORC space contains only noise in case of properly chosen measurement parameters (Table 1).

The saturating field B_{sat} of the FORC protocol resets the specimen to the same magnetic state before each curve, and must be larger than the maximum applied field $B_{cmax} + B_{umax}$. Setting B_{sat} to the maximum field allowed by the instrument is thereby not necessary, and even counterproductive, because it uses more ramping time and might activate high-coercivity viscous components that decay during the measurements. Instead, 1.2-1.5 times $B_{cmax} + B_{umax}$ is the most appropriate choice in most cases. The field step δB used for measurements is of paramount importance, since it determines the final resolution of the FORC diagram, which, in case of a constant smoothing factor SF, is given by $\Delta B = \delta B \times (SF + ½)$ (Egli et al., 2010; Egli, 2013, 2021). For instance, if ΔB = 3 mT is required for resolving the central ridge of a magnetofossil-bearing sediment, and SF = 4 for sufficient noise suppression, $\delta B \leq 0.7$ mT is required. Depending on the VSM control software, δB might be chosen directly, or through the total number N of measured curves. Finally the averaging time, t_m, of measurements should be chosen so that the hysteresis loop opening (expressed for instance by the difference between the two branches) is well defined over the entire range. In any case, any increase of t_m beyond 0.5 s does not produce a significant noise reduction. Because the total measurement time is proportional to $t_m/\delta B$, there is a practical limit to the increase of t_m for noise suppression and the decrease of δB for better resolution. Especially in the case of weak samples requiring high-resolution measurements, such as magnetofossil-bearing sediments, it is not possible to satisfy both criteria, since the measurement of a single curve should not exceed a few minutes, which is the typical timescale of instrumental drift, for a total measurement time that can reach 24 hours. In such cases, the desired signal-to-noise ratio must be achieved by stacking identical measurement sequences: this option is supported by VARIFORC (Egli, 2013).

Finally, additional options are provided for controlling some timing parameters of the FORC measurements. The time spent at the saturating field B_{sat} should be short (e.g. ≤ 1 s), to avoid the unnecessary activation of high-coercivity viscous components. The pause, t_r, at the reversal field controls the response of viscous particles to the FORC protocol, with larger pauses introducing a stronger timing asymmetry and thus a larger offset

of certain FORC features such as the central ridge (Berndt et al., 2018; Egli, 2021; Wagner et al., 2021). Even if the timing asymmetry is of no interest, a minimum t_r should be chosen to enable a sufficient field stabilization after the rapid ramping from positive saturation to B_r. The typical stabilization time for electromagnet-based VSM is of the order of 1 s. Shorter values of t_r introduce artifacts along the left limit of the FORC space (B_c = 0), which might be confused with the vertical ridge caused by thermal relaxation effects (Pike et al., 2001). A more robust control of the VSM behaviour at B_r is possible with the new Lake Shore 8600 VSM, including the complete avoidance of field overshooting problems (Egli, 2021; Wagner et al., 2021), as well as the ability of reaching fields > 2.5 T.

The choice of suitable measurement parameters depends also on the usage of FORC measurements. For instance, in case of FORC measurements for FORC-PCA analysis (Lascu et al., 2015), which typically involve a large number of samples with a common origin (e.g. a sediment core), the tradeoff between measurement speed and quality is shifted towards speed by choosing sub-optimal resolution and a FORC range that does not completely enclose the features of interest, since a considerable noise reduction is achieved at the endmember level. On the other hand, measurement quality and a sufficiently extended measurement range should be prioritized for the in-depth characterization of few selected samples, so that subtle low-amplitude or quasi-1D key features can be resolved. Notable examples include the central ridge and its offset, the low-amplitude external margins of the FORC functions, which contribute significantly to the total magnetization because of their large extension over B_c and B_u, and negative low-amplitude contributions caused by reversible magnetic moment rotation and by mean interaction fields (Egli, 2021). Such key features also require a proper processing, which unavoidably includes field-dependent smoothing, as in the VARIFORC protocol (Egli, 2013, 2021; Heslop et al., 2020). In case of time consuming FORC measurements (of many samples for FORC-PCA, or high-resolution-low-noise), regardless of lithology/material, it is generally recommended to make a rapid (~1 h) preliminary FORC measurement that fully characterizes the details of the magnetic particle system at hand. Finally, non-linear color scales and properly chosen contour levels are needed to represent high- and low amplitude features of the FORC diagram. Quantile contour lines, a new feature of VARIFORC (Egli, 2021) enable to highlight all features according to their relative contribution to the total magnetization.

Interpretation of characteristic FORC features

FORC diagrams can be essentially understood as a 2D mapping of transitions between magnetic states that occur upon sweeping the magnetic field from positive to negative saturation and vice-versa. As such, they convey much more detailed information than coercivity distributions, which can be understood as a 1D representation of the same transitions, or bulk parameters, which only express certain collective states of all magnetic particles in the specimen. Transitions between well-defined magnetic states, such the positive and negative state of uniaxial SD particles, vortex and SD states in small PSD particles, and pinned domain wall positions in MD particles, generate specific, localized, and well recognizable signatures in the FORC diagram, such as ridges and lobes. Some of these features, as for instance the central ridge of non-interacting SD crystals, maintain their characteristics in natural particle assemblages, where they can be identified even when superimposed on other magnetic components, while other features, such as the lobes of SD-vortex transitions in small PSD particles merge into a continuous background that extends over large parts of the FORC space. As with any other magnetic measurement, the interpretation of FORC diagrams is not always unique; however, the combination of magnetic mineralogy, domain state, and accessory characteristics such as size/shape distributions, presence of crystal defects, and magnetostactic or exchange interactions create some typical collective signatures that recur in natural samples. Our knowledge on such signatures is rapidly evolving, thanks to combined approaches that involve numerical and physical/chemical unmixing, sample comparison, and micromagnetic modelling (Roberts et al., 2014; Lascu et al., 2018; Egli, 2021). One of the main factors that control FORC signatures is the domain state of magnetic particles, which is discussed in the following.

Uniaxial SD particles

High-precision FORC models have been developed for uniaxial SD (UNISD) particles (Newell, 2005), and for UNISD particle assemblages with weak dipolar interactions (Egli, 2006). Such models are the only physical approximation of the Preisach-Néel model (Néel, 1958), where each point of the FORC diagram with coordinates (B_c, B_u) represents a magnetic particle with a rectangular hysteresis loop (the so-called hysteron) with coercive field B_c, horizontally biased by the interaction field B_u. In case of negligible magnetostatic interactions, the hysteresis loops of individual particles, which are curved instead of rectangular as in the Preisach-Néel model, are unbiased (B_u=0), so that the FORC function is concentrated in an infinitely sharp ridge $\rho_{cr}(B_c, B_u = 0)$, which is commonly referred to as the central ridge. The curvature of the hysteresis loops of individual particles, which is due to the reversible rotation of the particle's magnetic moments in the applied field, produces an additional contribution to the FORC diagram consisting of a continuous function that extends over the lower quadrant (B_u = 0), and is antisymmetric with respect to the $B_u = -B_u$ diagonal, with negative amplitudes below the diagonal and positive above (Newell, 2005). The FORC signature of non-interacting UNISD particles has long been overlooked, due to the fact that most synthetic SD particles are clustered and thus strongly interacting, and because the central ridge requires high-resolution measurements to be resolved, when superimposed on other contributions (Egli et al., 2010). Fig. 3 shows the first example of

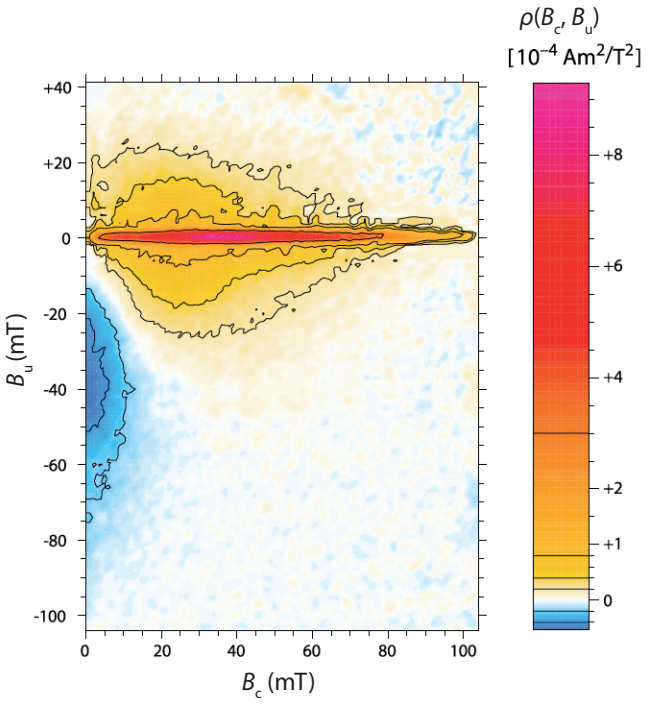

Figure 3. First FORC diagram measured for magnetotactic bacteria-bearing sediment modified after Egli et al. (2010). A central ridge and a negative distribution over $B_u < 0$, both non-interacting SD features modeled by Newell (2005), are clearly distinguishable, in addition to a broader positive distribution over the B_c axis, see text for details.

this signature obtained with a high-resolution measurement protocol from a lake sediment sample. The features of the FORC model calculated by Newell (2005) are clearly distinguishable: the central ridge along $B_u = 0$, and negative contributions below the $B_u = -B_u$ diagonal. Additional contributions in the upper quadrant, which will be discussed in the next section, are also evident.

High-resolution FORC measurements revealed that the central ridge is a common signature of marine and freshwater sediments (Roberts et al., 2012), where it is mainly associated with the fossil remainders of magnetotactic bacteria, as well as soils (Egli, 2021; Geiss et al., 2008) and ferromanganese deposits (Oda et al., 2018; Yuan et al., 2020). It is rarely encountered in rocks, because of the tendency for (titano)magnetite particles to grow beyond the SD size limit and to form patterned aggregates. A notable exception is represented by the Tiva Canyon Tuff (Berndt et al., 2018), which for this reason has been used by the IRM as a reference material for its SD properties.

Magnetofossils

As suggested by the coercivity components found in the central ridge (Egli et al., 2010; Heslop et al., 2014) and by TEM observations, the signature of non-interacting UNISD particles in many freshwater and marine sediments is mainly produced by fossilized chains of magnetosomes, known as magnetofossils, once produced by magnetotactic bacteria living in sediment or in the overlying water column. Fossil magnetosome chains are typically isolated within the sediment matrix, because the cell body first (Moskowitz et al., 1993), and then the sediment matrix, prevent the formation of clusters, which, instead, form upon cell dissolution in water (Kobayashi et al., 2006). Isolated chains of mature magnetosomes are magnetically equivalent to UNISD particles because all crystals in a chain switch at the same critical field (Hanzlik et al., 2002; Penninga et al., 1995). An exception is represented by magnetotactic bacteria containing magnetosome chain bundles or clusters (e.g., Faivre & Schüler, 2008; Hanzlik et al., 2002). Recent micromagnetic simulations (Amor et al., 2021) show that multi-stranded chains, either native, or resulting from the fold-collapse of single chains, produce, in addition to the classical FORC signature of non-interacting SD particles, a signature similar to that of strongly interacting SD particles, which is often visible in the upper quadrant of the FORC diagrams of magnetofossil-rich sediments (e.g., Fig. 3) (Ludwig et al., 2013). Unlike the case of SD particle clusters, however, the remanence ratio M_{rs}/M_s remains close to the value of 0.5 expected for non-interacting, randomly oriented UNISD. This difference results from multi-stranded chains maintaining a strongly uniaxial anisotropy, even if strong interactions occur between strands.

Thermal relaxation, viscous effects and interactions of SD particles

Thermal activations produce a slight broadening of the central ridge, which is related to the statistical nature of the switching field (Egli, 2006). Furthermore, since more time is spent at negative reversal fields than in positive fields during FORC measurements, thermally activated SD particles that have been switched to negative saturation in the reversal field B_r require a slightly larger positive field B to be switched back to positive saturation. This produces a small upward shift of the central ridge (Berndt et al., 2018), to an extent that depends on the energy barrier of the particles, and thus on their size, and on the timing of the measurement protocol, especially the pause t_r at the reversal field. In the case of typical high-resolution measurement parameters (δB = 0.5 mT, t_r = 1 s), the central ridge offset is of the order of 0.5 mT. This offset has been recently used to constrain the coercivity range of needle-shaped giant magnetofossils in sediments from the Paleocene-Eocene thermal maximum (Wagner et al., 2021). Additional thermal relaxation effects appear for particles close to the lower limit of the SD stability range. As this limit is approached, the switching fields of the particles decrease and the central ridge peak moves towards $B_c = 0$ as a consequence of the progressive closure of the hysteresis loop (Lanci & Kent, 2018). This is accompanied by a vanishing of the negative lobe in the lower quadrant, as the hysteresis loops of individual particles become more squared through switching in lower fields. At the same time, a vertical ridge along the left limit of the FORC diagram ($B_c = 0$) starts to form in the lower quadrant, due to the continuing thermally activated switching of SD particles to negative saturation while the applied field is still close to the reversal field (Lanci & Kent, 2018; Pike et al., 2001). The amplitude of this ridge is strongly dependent on the pause at reversal field B_r, the more time is spent

at B_r, the more particles are switched before the corresponding curve is measured, and not during the measurements. Measurement artifacts at B_r, which commonly arise when the applied field is not allowed to stabilize by a sufficiently long pause, also produce a vertical ridge that is often confused with that of viscous particles.

As the size of SD particles is further decreased to the point that they become superaparamagnetic (SP) the hysteresis loop becomes completely closed and all FORCs perfectly overlap. The lack of differences between measured curves means that the derivative of measurements with respect to B_r is zero, along with the FORC function. The exact particle size for this transition depends on the measurement temperature and time, according to the thermal relaxation theory of Néel (1949). The FORC signature of natural assemblages of non-interacting SD particles with a grain size distribution covering the SP and stable SD range thus contains a central ridge that extends to $B_c = 0$, produced by all particles that retain a remanent magnetization during the time required to measure a single curve, and a vertical ridge produced by a small fraction of viscous particles that switch in a time comparable with that required to obtain few measurement points. Typical examples include rapidly cooled rocks (Fig. 4), and well-developed soils (Egli, 2021), such as those of the Chinese Loess Plateau, where ~50% of all pedogenic magnetite is SP and the remaining part SD (Liu et al., 2005).

Magnetostatic interactions convert the central ridge into a function of finite thickness, which results in an appreciable vertical spread of the FORC function (Carvallo et al., 2005; Pike et al., 1999). In the Preisach-Néel model, horizontal and vertical profiles through the central maximum are identified with the switching field distribution $f(B_c)$ and the interaction field distribution $g(B_u)$, respectively, which in the simplest case where these distributions are represented by Gaussian functions, produce a FORC diagram with oval contours (Fig. 5). This type of FORC diagrams is characteristic for certain synthetic SD samples at higher concentrations (Carvallo et al., 2005; Pike et al., 1999), but $f(B_c)$ and $g(B_u)$ represent a collective behaviour of all particles rather than intrinsic distributions, where the distribution of interaction fields depends strongly on the bulk magnetic state of the assemblage (Muxworthy et al., 2004).

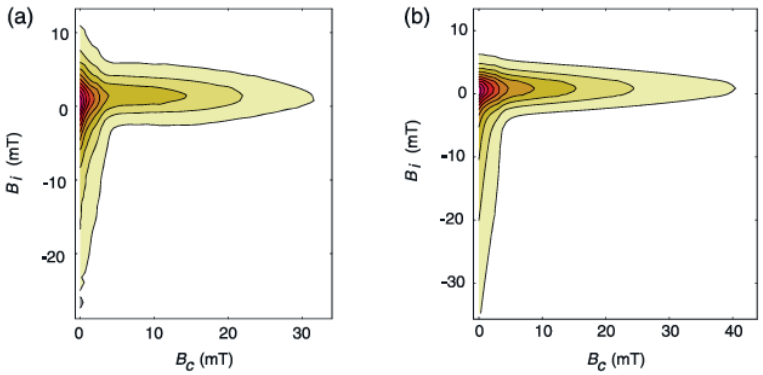

Figure 4. FORC distributions for: (a) particles near the SP to stable SD threshold size in a sample of the Tiva Canyon Tuff; (b) model results at 300 K, where most of the assemblage is in a thermally relaxed state. From Roberts et al.

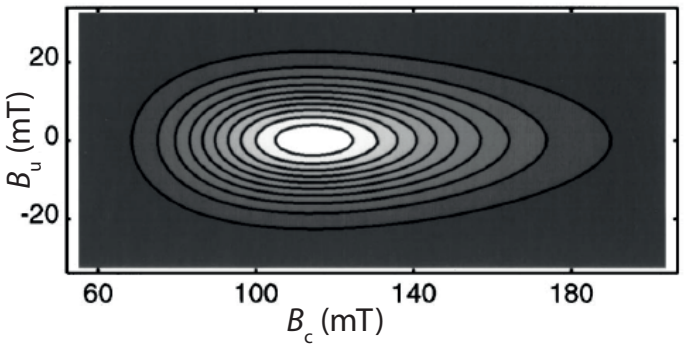

Figure. 5. FORC distribution calculated from a theoretical system of interacting SD particle data. Modified after Pike et al. (1999).

Weak magnetostatic interactions, on the other hand, produce a different FORC signature characterized by teardrop-shaped contour lines (Egli, 2006). This peculiar shape of contours is caused by a decrease of the width of $g(B_u)$ with increasing B_c. This can be understood by considering two SD particles: one whose coercivity is much lower than that of the other particles and one whose coercivity is much larger. The low-coercivity particle is switched by a small field change that will not affect the other particles and the stray field produced by them. In practice, the low-coercivity particle is switched in a constant local field that coincides with the B_u-coordinate of the FORC diagram, exactly as in the Preisach-Néel model of interactions. Accordingly, many low-coercivity particles disseminated in the sample will "probe" the local interaction field at random places, and thus the effective interaction field distribution. This distribution coincides with the vertical profile of the FORC function taken at a small B_c. A high-coercivity particle, on the other hand, is switched in large fields after all other particles have been already switched. This means that the local interaction field during switching of the high-coercivity particle to positive saturation is antiparallel to the local interaction field during switching of the high-coercivity particle to negative saturation. The lack of a constant bias in the hysteresis loop of high-coercivity particles means that their B_u-coordinate in the FORC diagram is zero, as for non-interacting particles. For this reason, the high-coercivity end of the FORC diagram of weakly interacting particles becomes a sharp ridge.

Caution should be used when interpreting FORC signatures of magnetostatic interactions, as fundamental differences between apparently similar assemblages of SD particles might be evident only when considering also the bulk hysteresis properties. For instance, the FORC signature of collapsed magnetosome chains produced in aqueous solution (Li et al., 2012) display a combination of central ridge and teardrop-shaped contours that is similar to that of magnetofossil-rich sediments (e.g., Fig. 3), despite the large differences in M_{rs}/M_s. Other complications arise in natural samples from the fact that the distribution of SD particles might not be homogeneous, so that not all particles necessarily interact with each other. For instance, uncorrelated switching and interaction field distributions could be generated in sediments containing heterogeneous clusters of SD particles formed for instance around reduction spots in sedi-

ments (Egli, 2021).

Vortex-state and pseudo single domain (PSD) grains

Magnetic properties of ferrimagnetic particles are strongly size-dependent, with clear limits defined for SD and MD particles. However, a range of particle sizes possess intermediate properties, which have been referred to as pseudo-single domain (PSD) (Stacey, 1961, 1962), e.g., ~0.2-2 μm for magnetite, which, while too large to be SD, have a magnetization that is too intense and stable for MD particles. PSD grains are the most common remanence carriers capable of recording the Earth magnetic field. Applied to magnetic properties, "PSD" describes a continuous transition between SD and MD endmembers, as defined, for example, by the hysteresis parameters M_{rs}/M_s and B_{cr}/B_c on a Day plot (Day et al., 1977), which are limited by $0.02 < M_{rs}/M_s < 0.5$ and $2 < B_{cr}/B_c < 5$. However, the PSD range can also be populated by strongly interacting SD particles, as well as binary/ternary mixtures of SP, SD, and MD particles. It is therefore not surprising that most geologic materials plot within the PSD range, with lower and upper M_{rs}/M_s limits given by theoretical SD-MD and SD-SP mixing trends, respectively. A similar ambiguity exists with any other domain-state-indicator based on bulk magnetic parameters, so that the term 'PSD behavior' instead of 'PSD particles' is more appropriate for describing bulk magnetic measurements that do not unambiguously indicate a SD or a MD signature (Egli, 2021).

However, despite the indefiniteness of PSD-like magnetic properties, there is a well-defined third magnetic state for magnetite particles with intermediate size ranges, which explains the PSD behavior not in terms of endmember mixtures. If magnetite particles are too large to be homogeneously magnetized, but too small to accommodate a domain wall, they will host a magnetic vortex (single vortex, SV) in which the magnetization vectors form a circular pattern around a "vortex tube" that acts to reduce the stray field energy of the particle (e.g. Tauxe et al., 2002). Magnetite particles feature magnetic vortices over a range of sizes, and sometimes a few magnetic vortices coexist in particles with irregular shapes, especially if elongated. As the particle size increases, the volume outside the vortex tubes tends to split into regions that can be effectively regarded as magnetic proto-domains separated by proto-domain-walls, in which the magnetization vectors rotate from one easy axis to the other. As the crystal size increases further these structures progressively evolve into classic domains and domain walls, respectively (Nagy et al., 2019).

Analogy to SD particles, the orientation of the vortex tube is stabilized by magnetocrystalline anisotropy and by crystal shape. Therefore, the vortex tube, which is the only feature contributing significantly to the total magnetic moment of the particle, behaves essentially like a SD particle, granting the magnetization stability sought in paleomagnetism (Nagy et al., 2017). On the other hand, the application of large external fields favors the transition from a SV-state to a SD-state, which, however, might not continue to exist metastably once the field is

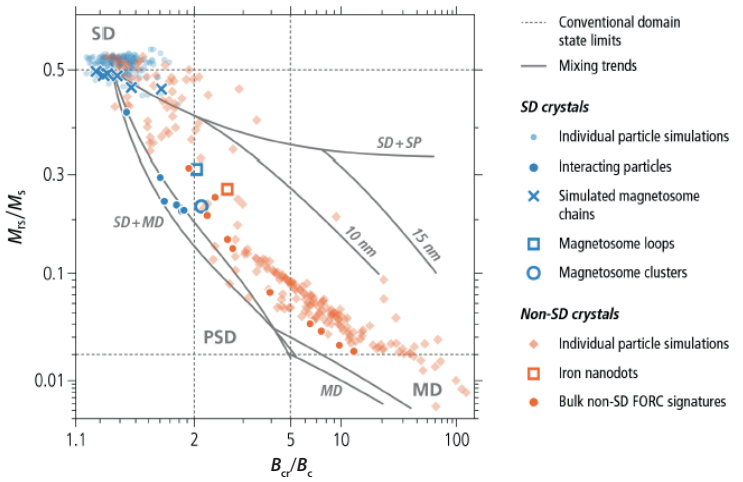

Fig 6. Day plot from Egli (2021). Filled dots represent measurements of bulk samples containing (1) SD particles with increasing degrees of magnetostatic interactions, in blue, and (2) magnetite particles with a PSD or MD FORC signature in orange. Small diamonds represent micromagnetic simulations of individual silicate-hosted magnetite crystals whose exact shape has been determined using focused ion-beam nanotomography by Nikolaisen et al. (2020). The domain states of these particles (SD or PSD) have been determined according to the presence or the lack of magnetic vortices in simulated hysteresis loops. Large symbols represent the bulk properties of particle assemblages with well-defined properties, which include, in the case of SD particles: micromagnetic simulations of magnetosome chains, measurements of looped chains of equidimensional magnetosomes produced by genetically modified bacteria, measurements of small clusters of equidimensional magnetosomes; and in the case of single-vortex particles: measurements of metallic iron nanodots (see Egli (2021) for details on these data).

removed. Depending on the stability of the SD state in zero field, particles can exhibit an elevated remanent magnetization typical of truly SD particles, expressed by Mrs/Ms values close to 0.5, or a much lower remanent magnetization arising from the vortex tubes, with MD-like M_{rs}/M_s values. Micromagnetic models of individual magnetite particles with shapes digitized from focused ion-beam nanotomography reveal that individual crystals hosting one or two magnetic vortices yield hysteresis loops that span all three domain regions of the Day diagram, with a grand average in the PSD range (Nikolaisen et al., 2020) (Fig. 6). Particles with metastable SD-like remanent magnetizations are characterized by B_{cr}/B_c values not exceeding 3: above this threshold, the magnetizations of most individual particles drop to $M_{rs}/M_s \approx 0.45\ (B_{cr}/B_c)^{-1}$. On a logarithmic scale, this trend is parallel to that of MD particles, which are characterized by 8 times smaller remanence ratios (Fig. 6).

Unlike SD particles, where all types of magnetizations rely on only one type of magnetic state (the SD state), SV particles can display two different types of magnetic states, which are preferentially selected by different magnetization acquisition mechanism, and which are characterized by different stabilities against thermal activations and external fields. For instance, a thermoremanent magnetization (TRM) preferentially selects magnetic states with lowest energy in zero fields (e.g. SV), while an isothermal remanent magnetization (IRM) selects magnetic states with maximum magnetic moment, that are still stable in zero field (e.g., SD). Since the field required to nucleate a SD-to-vortex transition

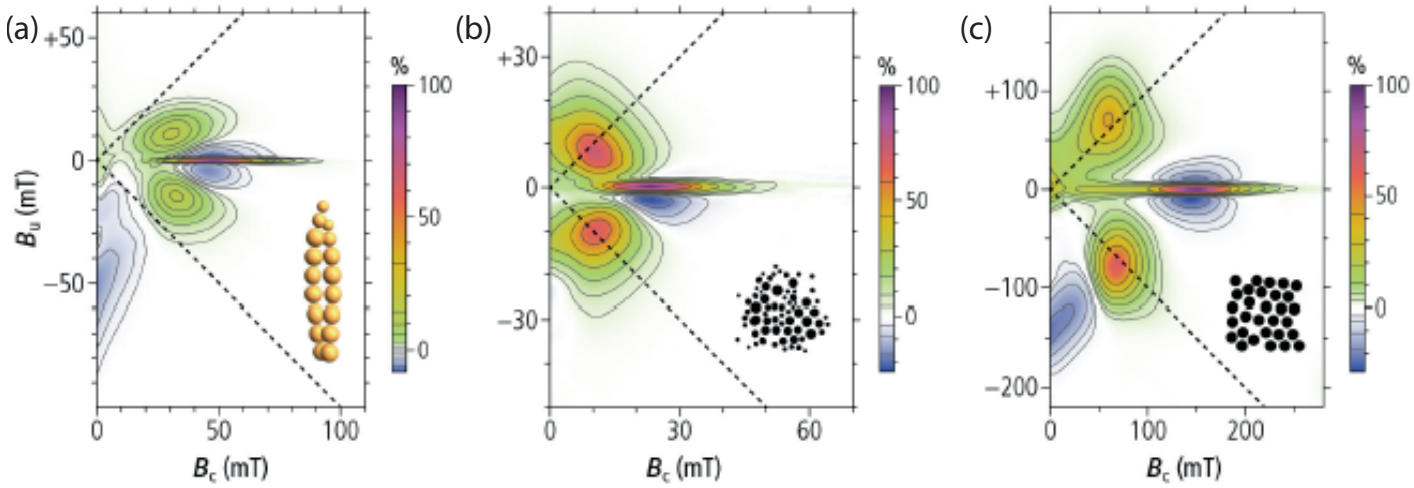

Fig. 7. FORC diagrams of three magnetic systems possessing two pairs of stable magnetic states with high and low magnetic moment, respectively, from Egli (2021). The dashed lines indicate the limits of the memory region, or zone 3: (a) Numerical model of randomly oriented, double-stranded chains of equidimensional SD magnetosomes formed from the fold-collapse of single-stranded chains (an example is shown in the inset); (b) Sample of SD magnetosome cluster-forming bacteria (an example is shown in the inset); (c) Metallic iron nanodots with 67 nm diameter. In (a-b) individual particles are SD, and the existence of low- and high-moment states depends on the magnetic moment arrangement. In (c) individual particles possess SD-like and vortex states (see Egli (2021) for details on these data).

can be arbitrarily small, while the contrary is not true, a PSD IRM is generally less stable than a PSD TRM.

Experimental work on Fe nanoparticles with grain sizes slightly larger than the upper SD limit showed that hysteresis properties are shaped by the transition sequences $SD^+ \rightarrow SV^+$ (vortex nucleation)$\rightarrow SD^-$ (vortex annihilation) along the upper branch and $SD^- \rightarrow SV^-$ (vortex nucleation) $\rightarrow SD^+$ (vortex annihilation) along the lower branch. That is, when the magnetization is decreased from saturation, a vortex will form at a given nucleation field. If a FORC measurement is started from this state, this vortex will eventually annihilate, but not necessarily at the same absolute field value at which it was nucleated. The different nucleation/annihilation fields of positive and negative SV states creates a complex multi-lobe FORC signature (Fig. 7). This signature is common to all isolated magnetic systems (individual particles or structures made of strongly coupled particles) that feature exactly two types of magnetic states: a high-moment state analogous to that of SD particles, and a low-moment state analogous to a SV. For instance, the FORC diagrams of a homogeneous assemblage of double-stranded magnetosome chains or small clusters of equidimensional SD particles are characterized by a "butterfly" signature identical to that of the SV particles shown in Fig. 7 (Egli, 2021; Pike & Fernandez, 1999).

The multi-lobe structure is characterized by a central ridge, surrounded by two positive lobes centered at lower values of B_c, and one or two negative, smaller lobes centered at higher values of B_c. All these features are clearly visible in Fig. 7. Additional features, such as the negative contributions below the $B_u = -B_c$ diagonal, and certain asymmetries between the upper and lower quadrant originate from the reversible rotation of SD or SV magnetic moments in the applied field. The positive lobe located above the central ridge is caused by the annihilation of a SV^+ state that was nucleated when sweeping the field from positive saturation to the reversal field. The remaining features are formed when measuring FORCs that start from the negative saturation state SD^-: the first irreversible transition $SD^- \rightarrow SV^-$ creates the lower positive lobe, and the second irreversible transition $SV^- \rightarrow SD^+$ contributes to the central ridge. The latter transition is located exactly on $B_u = 0$ because the first curve hosting this transition starts just after the symmetric opposed transition $SV^+ \rightarrow SD^-$ has occurred at the reversal field. Finally, the negative lobes are associated with the same SV^+ annihilations that cause the positive lobe above the central ridge, but "seen" from the differences between curves starting from the SD^- and SV^+ states, respectively, instead of the difference between curves starting from the SV^+ and SD^+ states (Egli, 2021; Pike & Fernandez, 1999).

Additional features related to reversible magnetization changes depend on the detailed magnetic configurations underlying the high- (SD) and low- (SV) moment states, and how these configurations change during FORC measurements between successive transitions. For instance, reversible vortex tube rotation produces two broad ridges along +45° lines: a positive one departing from the upper positive lobe, and a negative one departing from the lower positive lobe (Pike & Fernandez, 1999), both discernible in Fig. 7c. Overall, these reversible processes are responsible for observed asymmetries between the upper and lower quadrants of the FORC diagram. Other asymmetries, e.g., between negative lobes above and below the central ridge, depend on small differences between the annihilation fields of positive and negative low-moment states.

The location of the two positive lobes with respect to the memory region of the FORC diagram (right of the dashed lines in Fig. 7) determines whether the high-moment (SD) states are stable in zero field, therefore affecting M_{rs}/M_s. If the positive lobes are located fully within the memory region, M_{rs} is equivalent to a SD magnetization, yielding $M_{rs}/M_s = 0.5$ in case of randomly oriented particles with uniaxial anisotropy. If, on the contrary, the positive lobes are located fully outside the memory

region (that is, in the so-called transient region), M_{rs} is controlled by the low-moment magnetic states, the only ones that are stable in a zero field, yielding $M_{rs}/M_s << 0.5$. The sudden disappearance of stable high-moment configurations for particles with $B_{cr}/B_c > 3$ is clearly visible in the micromagnetic simulations of Nikolaisen et al. (2020), and marks the transition from PSD to a MD-like hysteresis behavior. Furthermore, these simulations do not show a systematic relation between individual particle sizes and their location in the Day diagram: for instance, the SD range is populated by single and multi-vortex particles.

Natural materials featuring all signatures shown in Fig. 7 are rare, since they require a tight control over all factors determining the nucleation/denucleation fields of low-moment states: dusty olivines containing Fe-Ni inclusions feature the central ridge, the two positive lobes, and one negative lobe below the central ridge (Lappe et al., 2011, 2013), similarly to hexagonal magnetite platelets produced by thermophilic iron-reducing bacteria (Zhao et al., 2017). More generally, magnetic particles with PSD behavior can have several more magnetic configurations in addition to the SD and SV ones discussed above, multiplying the number of irreversible transitions that will occur during hysteresis and FORC measurements. Additional configurations include multiple vortices (MV) and swirls, which are found preferentially in elongated particles (Lascu et al., 2018; Nikolaisen et al., 2020). Interestingly, the hysteresis properties of individual MV particles plot in the classic PSD range of the Day diagram, contrary to SV particles. During FORC measurements, discrete transitions occur between magnetic states, which are usually accompanied by a jump of the magnetic moment, and each state evolves reversibly between its nucleation and its annihilation field, determining the continuous part of magnetic moment changes. Transitions generate isolated, sharp peaks in the FORC diagram, which are preceded by a +45° ridge caused by reversible magnetization changes (Egli, 2021; Egli & Winklhofer, 2014). Because FORCs obtained from large collections of particles tend to be contained within the branches of the major hysteresis loop, most peaks are contained in a triangular region of the FORC diagram with vertices (0, $\pm B_s$) and ($+B_s$, 0), where B_s is the field amplitude at which the hysteresis closes (Fig. 8a). These discrete contributions merge into a continuous FORC function within the triangular region limited by B_s as the number of particles increase (Fig. 8b). Transitions contributing to the central ridge become comparatively rare as the number of magnetic states in each particle increases, until they are no longer distinguishable. Fig. 8 shows the emergence of the classic FORC signature of PSD particles from the micromagnetic models of individual particles in an obsidian sample (Lascu et al., 2018).

Most FORC diagrams of PSD particles retain a reminiscence of the SV signature, in particular the two posi-

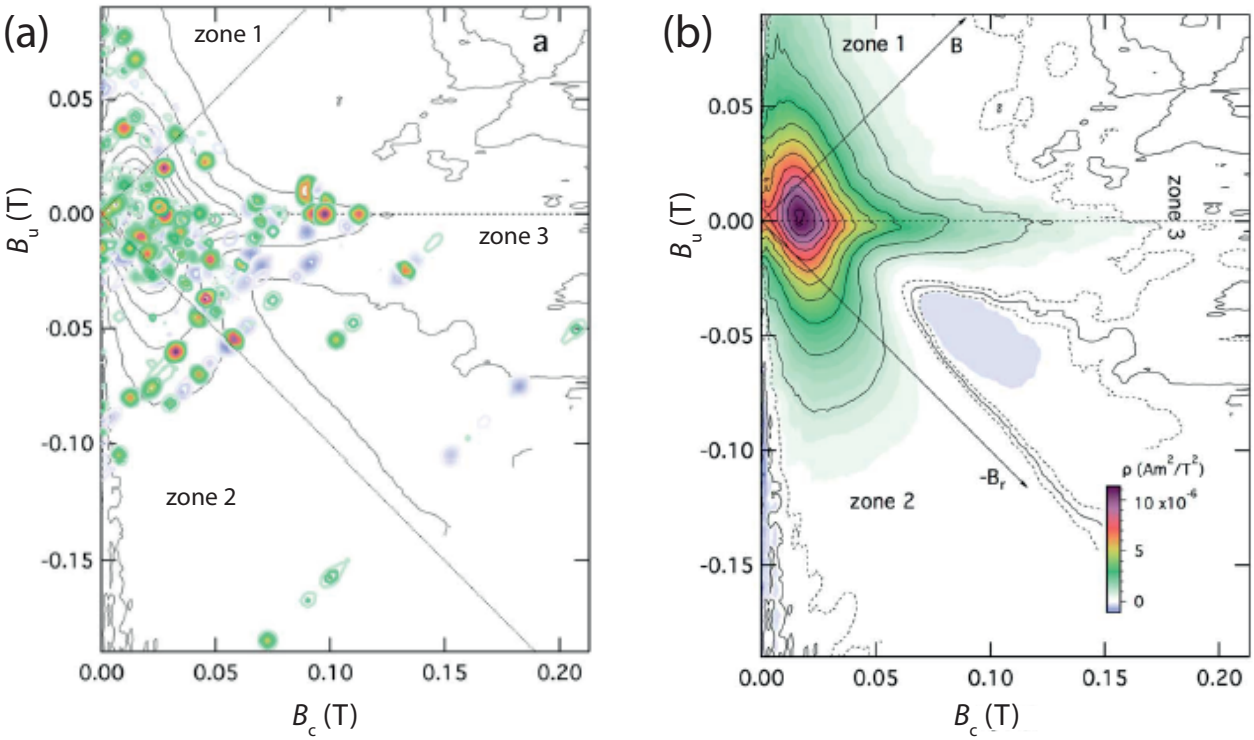

Fig. 8. Micromagnetic models of individual particles in an obsidian sample merging into the classic PSV FORC signature, from Lascu et al. (2018): (a) simulated positive and negative FORCs of few individual particles superimposed onto the contours of the experimental FORC diagram shown in panel (b); b) Experimental FORC for a natural obsidian sample containing interacting single vortex particles. The large number of particles contained in the bulk sample, compared to the simulations in (a) causes the FORC peaks to merge into a continuous background with more triangular, or tri-lobate, contour lines, as commonly observed for natural PSD assemblages. The upper lobe contours intersect the vertical axis at higher absolute values than those for the lower lobe, which intersect the vertical axis closer to the origin. The middle central-ridge-like lobe is narrower and extends just below the horizontal axis and there is a prominent negative region between this and the middle lobe. The strongest, broad, peak occurs at the intersection of the three lobes (see Lascu et al. (2018) for details).

tive lobes at lower coercivities, and a broadened central ridge at higher coercivities, which is probably affected by magnetostatic interactions (Lascu et al., 2015, 2018; Roberts et al., 2017). As noted by Lascu et al. (2018), the PSD signature contains a broad central peak at low coercivities, which is absent in SV particles. This peak, which is similar to that of interacting SD particles, appears to be associated with MV particles.

From PSD to multi domain (MD) grains

A sharp transition between the FORC signatures of natural PSD and MD magnetite particle assemblages does not exist. Instead, a continuous transition to the MD endmember, consisting in a vertical ridge close to $B_c = 0$ (Egli, 2021; Pike et al., 2001), is observed. This transition is characterized by an increase of the vertical extension of the FORC function and a migration of the central peak towards $B_c = 0$ (Fig. 9). This is consistent with the coexistence of domain walls and vortex cores, which, in equidimensional magnetite crystals, starts at around 1 µm (Lascu et al., 2018; A. R. Muxworthy & Dunlop, 2002; Nagy et al., 2017; Roberts et al., 2017). It is worth observing that a broadened form of the central ridge extending to relatively large coercivities persist in MD magnetite up to macroscopic sizes (Pike et al., 2001), and it is accompanied by a negative region located between the central ridge itself and the $B_c = -B_u$ diagonal in the lower quadrant (Fig. 9). Early FORC diagrams did not resolve this signature in natural materials, due its low amplitude, typically <5% of the central peak. Both signatures disappear upon annealing (Pike et al., 2001), which means that they must be affected by the presence of internal stress or crystal defects. Egli et al. (2021) noticed that the negative region in the lower quadrant is explainable by the presence of a mean demagnetizing field, which is compatible, in amplitude, with the internal demagnetizing field of magnetite particles (e.g., Dunlop & Özdemir, 1997). Egli (2021) speculates from this observation that the FORC signature of PSD-to-MD transitions is affected by the screening of PSD-like magnetic configurations, such as vortices, through parts of the particle's volume that are characterized by a MD behavior. This is also indirectly supported by the results of Nikolaisen et al. (2020): while there is no strong relation between grain size and type of magnetic states once the upper stability limit for SD particles is exceeded, the role of size is clearly seen in the relation between coercive field B_c and M_{rs}/M_s, with larger particles showing a trend that is compatible with a larger demagnetizing factor.

References

Amor, M., Wan, J., Egli, R., Carlut, J., Gatel, C., Anderssen, I.M., et al. (2021). Magnetic flux closure in mutant magnetotactic bacteria elucidates a key signature of magnetofossils. Nature Communications, In review. https://doi.org/10.21203/rs.3.rs-187824/v1

Berndt, T. A., & Chang, L. (2019). Waiting for Forcot: Accelerating FORC Processing 100× Using a Fast-Fourier-Transform Algorithm. Geochemistry, Geophysics, Geosystems, 20(12), 6223–6233. https://doi.org/10.1029/2019GC008380

Berndt, T. A., Chang, L., Wang, S., & Badejo, S. (2018). Time-Asymmetric FORC Diagrams: A New Protocol for Visualizing Thermal Fluctuations and Distinguishing Magnetic Mineral Mixtures. Geochemistry, Geophysics, Geosystems, 19(9), 3056–3070. https://doi.org/10.1029/2018GC007669

Carvallo, C., Dunlop, D. J., & Özdemir, Ö. (2005). Experimental comparison of FORC and remanent Preisach diagrams. Geophysical Journal International, 162(3), 747–754. https://doi.org/10.1111/j.1365-246X.2005.02688.x

Chen, A. P., Egli, R., & Moskowitz, B. (2005). A FORC in the road? The IRM Quarterly, 15(3), 1–11.

Day, R., Fuller, M., & Schmidt, V. A. (1977). Hysteresis properties of titanomagnetites: grain-size and compositional dependence. Physics of the Earth and Planetary Interiors, 13, 260–267. https://doi.org/10.1016/0031-9201(77)90108-X

Dumas, R. K., Li, C.-P., Roshchin, I. V., Schuller, I. K., & Liu, K. (2007). Magnetic fingerprints of sub-100 nm Fe dots. Physical Review B, 75(134405), 1–5.

Dunlop, D. J., & Özdemir, Ö. (1997). Rock Magnetism: Fundamentals and Frontiers (p. 573). Cambridge: Cambridge

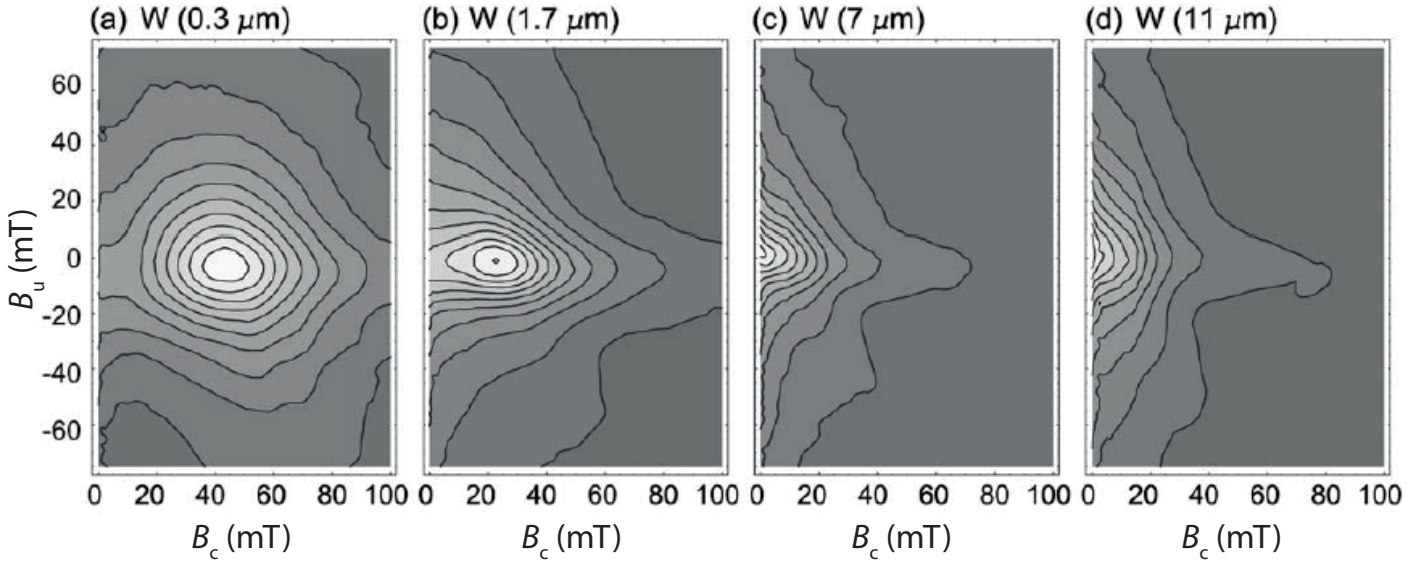

Figure 9. FORC distributions for synthetic samples ranging from PSD to MD: a) 0.3 µm; b) 1.7 µm; c) 7 µm; d) 11 µm. With increased grain size the main distribution shifts to lower coercivity and the FORC contours become increasingly parallel to the B_u axis, see text for details. Modified after Muxworthy and Dunlop (2002).

University Press.
Egli, R. (2006). Theoretical aspects of dipolar interactions and their appearance in first-order reversal curves of thermally activated single-domain particles. Journal of Geophysical Research: Solid Earth, 111(12), 1–18. https://doi.org/10.1029/2006JB004567
Egli, R. (2013). VARIFORC: An optimized protocol for calculating non-regular first-order reversal curve (FORC) diagrams. Global and Planetary Change, 110, 302–320. https://doi.org/10.1016/j.gloplacha.2013.08.003
Egli, R. (2021). Magnetic Characterization of Geologic Materials with First-Order Reversal-Curves. In V. Franco & B. Dodrill (Eds.), Magnetic Measurement Techniques for Materials Characterization, in press. Springer Nature Publishing Group.
Egli, R., & Winklhofer, M. (2014). Recent developments on processing and interpretation aspects of First-Order Reversal curves (FORC). Uchenye Zapiski Kazanskogo Universiteta. Seriya Estestvennye Nauki, 156(1), 14–53.
Egli, R., Chen, A. P., Winklhofer, M., Kodama, K. P., & Horng, C.-S. (2010). Detection of noninteracting single domain particles using first-order reversal curve diagrams. Geochemistry, Geophysics, Geosystems, 11(1), n/a-n/a. https://doi.org/10.1029/2009GC002916
Faivre, D., & Schüler, D. (2008). Magnetotactic Bacteria and Magnetosomes. Chemical Reviews, 108(11), 4875–4898. https://doi.org/10.1021/cr078258w
Geiss, C. E., Egli, R., & Zanner, C. W. (2008). Direct estimates of pedogenic magnetite as a tool to reconstruct past climates from buried soils. Journal of Geophysical Research, 113(B11), B11102. https://doi.org/10.1029/2008JB005669
Hanzlik, M., Winklhofer, M., & Petersen, N. (2002). Pulsed-field-remanence measurements on individual magnetotactic bacteria. Journal of Magnetism and Magnetic Materials, 248(2), 258–267. https://doi.org/10.1016/S0304-8853(02)00353-0
Harrison, R. J., & Feinberg, J. M. (2008). FORCinel: An improved algorithm for calculating first-order reversal curve distributions using locally weighted regression smoothing. Geochemistry, Geophysics, Geosystems, 9(5), n/a-n/a. https://doi.org/10.1029/2008GC001987
Hejda, P., & Zelinka, T. (1990). Modeling of hysteresis processes in magnetic rock samples using the Preisach diagram. Physics of the Earth and Planetary Interiors, 63(1–2), 32–40.
Heslop, D., & Roberts, A. P. (2012). A method for unmixing magnetic hysteresis loops. Journal of Geophysical Research: Solid Earth, 117(B3), 1–13. https://doi.org/10.1029/2011JB008859
Heslop, D., Roberts, A. P., & Chang, L. (2014). Characterizing magnetofossils from first-order reversal curve (FORC) central ridge signatures. Geochemistry, Geophysics, Geosystems, 15(6), 2170–2179. https://doi.org/10.1002/2014GC005291
Heslop, D., Roberts, A. P., Oda, H., Zhao, X., Harrison, R. J., Muxworthy, A. R., et al. (2020). An Automatic Model Selection-Based Machine Learning Framework to Estimate FORC Distributions. Journal of Geophysical Research: Solid Earth, 125(10). https://doi.org/10.1029/2020JB020418
Jackson, M., & Solheid, P. (2010). On the quantitative analysis and evaluation of magnetic hysteresis data. Geochemistry, Geophysics, Geosystems, 11(4), n/a-n/a. https://doi.org/10.1029/2009GC002932
Kobayashi, A., Kirschvink, J. L., Nash, C. Z., Kopp, R. E., Sauer, D. A., Bertani, L. E., et al. (2006). Experimental observation of magnetosome chain collapse in magnetotactic bacteria: Sedimentological, paleomagnetic, and evolutionary implications. Earth and Planetary Science Letters, 245(3–4), 538–550. https://doi.org/10.1016/j.epsl.2006.03.041
Lanci, L., & Kent, D. V. (2018). Forward Modeling of Thermally Activated Single-Domain Magnetic Particles Applied to First-Order Reversal Curves. Journal of Geophysical Research: Solid Earth, 123(5), 3287–3300. https://doi.org/10.1002/2018JB015463
Lappe, S.-C. L. L., Church, N. S., Kasama, T., da Silva Fanta, A. B., Bromiley, G., Dunin-Borkowski, R. E., et al. (2011). Mineral magnetism of dusty olivine: A credible recorder of pre-accretionary remanence. Geochemistry, Geophysics, Geosystems, 12(12), n/a-n/a. https://doi.org/10.1029/2011GC003811
Lappe, S.-C. L. L., Feinberg, J. M., Muxworthy, A., & Harrison, R. J. (2013). Comparison and calibration of non-heating paleointensity methods: A case study using dusty olivine. Geochemistry, Geophysics, Geosystems, 14(7), 2143–2158. https://doi.org/10.1002/ggge.20141
Lascu, I., Harrison, R. J., Li, Y., Muraszko, J. R., Channell, J. E. T., Piotrowski, A. M., & Hodell, D. A. (2015). Magnetic unmixing of first-order reversal curve diagrams using principal component analysis. Geochemistry, Geophysics, Geosystems, 16(9), 2900–2915. https://doi.org/10.1002/2015GC005909
Lascu, I., Einsle, J. F., Ball, M. R., & Harrison, R. J. (2018). The Vortex State in Geologic Materials: A Micromagnetic Perspective. Journal of Geophysical Research: Solid Earth, 123(9), 7285–7304. https://doi.org/10.1029/2018JB015909
Li, J., Wu, W., Liu, Q., & Pan, Y. (2012). Magnetic anisotropy, magnetostatic interactions and identification of magnetofossils. Geochemistry, Geophysics, Geosystems, 13(12). https://doi.org/10.1029/2012GC004384
Liu, Q., Torrent, J., Maher, B. A., Yu, Y., Deng, C., Zhu, R., & Zhao, X. (2005). Quantifying grain size distribution of pedogenic magnetic particles in Chinese loess and its significance for pedogenesis. Journal of Geophysical Research: Solid Earth, 110(B11), 1–7. https://doi.org/10.1029/2005JB003726
Ludwig, P., Egli, R., Bishop, S., Chernenko, V., Frederichs, T., Rugel, G., et al. (2013). Characterization of primary and secondary magnetite in marine sediment by combining chemical and magnetic unmixing techniques. Global and Planetary Change, 110, 321–339. https://doi.org/10.1016/j.gloplacha.2013.08.018
Moskowitz, B. M., Frankel, R. B., & Bazylinski, D. A. (1993). Rock magnetic criteria for the detection of biogenic magnetite. Earth and Planetary Science Letters, 120(3–4), 283–300. https://doi.org/10.1016/0012-821X(93)90245-5
Muxworthy, A., Heslop, D., & Williams, W. (2004). Influence of magnetostatic interactions on first-order-reversal-curve (FORC) diagrams: a micromagnetic approach. Geophysical Journal International, 158(3), 888–897. https://doi.org/10.1111/j.1365-246X.2004.02358.x
Muxworthy, A. R., & Dunlop, D. J. (2002). First-order reversal curve (FORC) diagrams for pseudo-single-domain magnetites at igh temperature. Earth and Planetary Science Letters, 203(1), 369–382. https://doi.org/10.1016/S0012-821X(02)00880-4
Nagy, L., Williams, W., Muxworthy, A. R., Fabian, K., Almeida, T. P., Conbhuí, P. Ó., & Shcherbakov, V. P. (2017). Stability of equidimensional pseudo–single-domain magnetite over billion-year timescales. Proceedings of the National Academy of Sciences, 114(39), 10356–10360. https://doi.org/10.1073/pnas.1708344114
Nagy, L., Williams, W., Tauxe, L., & Muxworthy, A. R. (2019). From Nano to Micro: Evolution of Magnetic Do-

main Structures in Multidomain Magnetite. Geochemistry, Geophysics, Geosystems, 20(6), 2907–2918. https://doi.org/10.1029/2019GC008319

Néel, L. (1949). Théorie du traînage magnétique des ferromagnétiques en grains fins avec applications aux terres cuites. Annales de Geophysique, 5(99–136).

Néel, L. (1958). Sur les effets d'un couplage entre grains ferromagnétiques. C.R. Acad. Sci., 246, 2313–2319.

Newell, A. J. (2005). A high-precision model of first-order reversal curve (FORC) functions for single-domain ferromagnets with uniaxial anisotropy. Geochemistry, Geophysics, Geosystems, 6(5). https://doi.org/10.1029/2004GC000877

Nikolaisen, E. S., Harrison, R. J., Fabian, K., & McEnroe, S. A. (2020). Hysteresis of Natural Magnetite Ensembles: Micromagnetics of Silicate-Hosted Magnetite Inclusions Based on Focused-Ion-Beam Nanotomography. Geochemistry, Geophysics, Geosystems, 21(11), 1–20. https://doi.org/10.1029/2020GC009389

Oda, H., Nakasato, Y., & Usui, A. (2018). Characterization of marine ferromanganese crust from the Pacific using residues of selective chemical leaching: identification of fossil magnetotactic bacteria with FE-SEM and rock magnetic methods. Earth, Planets and Space, 70(1), 165. https://doi.org/10.1186/s40623-018-0924-3

Penninga, I., de Waard, H., Moskowitz, B. M., Bazylinski, D. A., & Frankel, R. B. (1995). Remanence measurements on individual magnetotactic bacteria using a pulsed magnetic field. Journal of Magnetism and Magnetic Materials, 149(3), 279–286. https://doi.org/10.1016/0304-8853(95)00078-X

Pike, C. R., & Fernandez, A. (1999). An investigation of magnetic reversal in submicron-scale Co dots using first order reversal curve diagrams. Journal of Applied Physics, 85(9), 6668–6676. https://doi.org/10.1063/1.370177

Pike, C. R., Roberts, A. P., & Verosub, K. L. (1999). Characterizing interactions in fine magnetic particle systems using first order reversal curves. Journal of Applied Physics, nisms using FORC diagrams. Physics of the Earth and Planetary Interiors, 126(1–2), 11–25. https://doi.org/10.1016/S0031-9201(01)00241-2

Preisach, F. (1935). Über die magnetische Nachwirkung. Zeitschrift Fur Physik, 94(5–6), 277–302. https://doi.org/10.1007/BF01349418

Roberts, A. P., Liu, Q., Rowan, C. J., Chang, L., Carvallo, C., Torrent, J., & Horng, C.-S. (2006). Characterization of hematite (α -Fe 2 O 3), goethite (α -FeOOH), greigite (Fe 3 S 4), and pyrrhotite (Fe 7 S 8) using first-order reversal curve diagrams. Journal of Geophysical Research: Solid Earth, 111(B12), n/a-n/a. https://doi.org/10.1029/2006JB004715

Roberts, A. P., Chang, L., Heslop, D., Florindo, F., & Larrasoaña, J. C. (2012). Searching for single domain magnetite in the "pseudo-single-domain" sedimentary haystack: Implications of biogenic magnetite preservation for sediment magnetism and relative paleointensity determinations. Journal of Geophysical Research: Solid Earth, 117(B8), n/a-n/a. https://doi.org/10.1029/2012JB009412

Roberts, A. P., Heslop, D., Zhao, X., & Pike, C. R. (2014). Understanding fine magnetic particle systems through use of first-order reversal curve diagrams. Reviews of Geophysics, 52(4), 557–602. https://doi.org/10.1002/2014RG000462

Roberts, A. P., Almeida, T. P., Church, N. S., Harrison, R. J., Heslop, D., Li, Y., et al. (2017). Resolving the Origin of Pseudo-Single Domain Magnetic Behavior. Journal of Geophysical Research: Solid Earth, 122(12), 9534–9558. https://doi.org/10.1002/2017JB014860

Stacey, F. D. (1961). Theory of the magnetic properties of igneous rocks in alternating fields. Philosophical Magazine, 6(70), 1241–1260. https://doi.org/10.1080/14786436108243374

Stacey, F. D. (1962). A generalized theory of thermoremanence, covering the transition from single domain to multidomain magnetic grains. Philosophical Magazine, 7(83), 1887–1900. https://doi.org/10.1080/14786436208213853

Tauxe, L., Bertram, H. N., & Seberino, C. (2002). Physical interpretation of hysteresis loops: Micromagnetic modeling of fine particle magnetite. Geochemistry, Geophysics, Geosystems, 3(10), 1–22. https://doi.org/10.1029/2001GC000241

Wagner, C. L., Egli, R., Lascu, I., Lippert, P. C., Livi, K. J. T., & Sears, H. B. (2021). In situ magnetic identification of giant, needle-shaped magnetofossils in Paleocene–Eocene Thermal Maximum sediments. Proceedings of the National Academy of Sciences, 118(6), e2018169118. https://doi.org/10.1073/pnas.2018169118

Yuan, W., Zhou, H., Yang, Z., Hein, J. R., & Yang, Q. (2020). Magnetite magnetofossils record biogeochemical remanent magnetization in hydrogenetic ferromanganese crusts. Geology, 48(3), 298–302. https://doi.org/10.1130/G46881.1

Zhao, X., Roberts, A. P., Heslop, D., Paterson, G. A., Li, Y., & Li, J. (2017). Magnetic domain state diagnosis using hysteresis reversal curves. Journal of Geophysical Research: Solid Earth, 122(7), 4767–4789. https://doi.org/10.1002/2016JB013683

The IRM Quarterly

The *Institute for Rock Magnetism* is dedicated to providing state-of-the-art facilities and technical expertise free of charge to any interested researcher who applies and is accepted as a Visiting Fellow. Short proposals are accepted semi-annually in spring and fall for work to be done in a 10-day period during the following half year. Shorter, less formal visits are arranged on an individual basis through the Facilities Manager.

The *IRM* staff consists of **Subir Banerjee**, Professor/Founding Director; **Bruce Moskowitz**, Professor/Director; **Joshua Feinberg**, Assistant Professor/Associate Director; **Maxwell Brown, Peat Sølheid** and **Dario Bilardello**, Staff Scientists.

Funding for the *IRM* is provided by the **National Science Foundation**, the **W. M. Keck Foundation**, and the **University of Minnesota**.

The *IRM Quarterly* is published four times a year by the staff of the *IRM*. If you or someone you know would like to be on our mailing list, if you have something you would like to contribute (*e.g.*, titles plus abstracts of papers in press), or if you have any suggestions to improve the newsletter, please notify the editor:

Dario Bilardello
Institute for Rock Magnetism
University of Minnesota
150 John T Tate Hall
116 Church Street SE
Minneapolis, MN 55455-0128
phone: (612) 624-5049
e-mail: dario@umn.edu
www.irm.umn.edu

UNIVERSITY OF MINNESOTA

IRM